minerals

MDPI

Article

Origin of the Miaoling Gold Deposit, Xiong'ershan District, China: Findings Based on the Trace Element Characteristics and Sulfur Isotope Compositions of Pyrite

Simo Chen [1], Junqiang Xu [2,3,*], Yanchen Yang [1], Shijiong Han [1], Peichao Ding [3], Zhaoyang Song [4], Tianwen Chen [1] and Daixin Zhang [1]

[1] College of Earth Sciences, Jilin University, Changchun 130061, China; csm22@mails.jlu.edu.cn (S.C.); yyc@jlu.edu.cn (Y.Y.); hanshijiong@jlu.edu.cn (S.H.); chentw22@mails.jlu.edu.cn (T.C.); zdx22@mails.jlu.edu.cn (D.Z.)
[2] College of Geo-Exploration Science and Technology, Jilin University, Changchun 130061, China
[3] HeNan First Geology and Mineral Survey Institute, Luoyang 471023, China; dingpeichao1314@163.com
[4] Seventh Geological Brigade, Hubei Geological Bureau, Yichang 443100, China; 15754300623@163.com
* Correspondence: xvjunqiang@126.com

Abstract: The Xiong'ershan district is situated on the southern margin of the North China Craton (NCC) and located within the Qinling–Dabieshan Orogen's orogenic zone. It is adjacent to the XiaoQinling mining district and exhibits very favorable geological conditions for mineralization, as the district contains numerous gold deposits, positioning it as one of the key gold-producing areas of China. The Miaoling gold deposit is a hydrothermal deposit and is controlled by the Mesozoic nearly NS-trending fault. The ore bodies are hosted in the Mesoproterozoic Xiong'er Group of the Changcheng System of volcanic rocks, with reserves reaching large-scale levels. Pyrite is the main gold-bearing mineral and can be classified into four generations: early-stage fine- to medium-grained euhedral to subhedral cubic pyrite (Py1); medium- to coarse-grained euhedral to subhedral cubic granular pyrite in quartz veins (Py2a); fine-grained subhedral to anhedral disseminated pyrite in altered rocks (Py2b); and late-stage anhedral granular and fine-veinlet pyrite in later quartz veins (Py3). Through in situ trace element analysis of the pyrite using LA-ICP-MS, a positive correlation between Au and As was observed during the main mineralization stage; gold mainly exists as a solid solution within the pyrite lattice, and the ablation signal curve reflecting the intensity of trace element signals showed that gold also occurs as micron-scale mineral inclusions. The trace element content suggested a gradual increase in oxygen fugacity from Stage 1 to Stage 2, followed by a decrease from Stage 2 to Stage 3. The Co/Ni values in the pyrite (0.56 to 62.02, with an average of 12.34) exhibited characteristics of magmatic hydrothermal pyrite. The in situ sulfur isotope analysis of the pyrite using LA-MC-ICP-MS showed $\delta^{34}S$ values of 4.24‰ for Stage 1, −6.63‰ to −13.79‰ for Stage 2, and −4.31‰ to −5.15‰ for Stage 3. Considering sulfur isotope fractionation, the $\delta^{34}S$ value of the hydrothermal fluid during the main mineralization stage was calculated to be between 0.31‰ and 2.68‰.

Keywords: pyrite; trace elements; S isotope; LA-MC-ICP-MS; LA-ICP-MS; Miaoling gold deposit; North China Craton

check for updates

Academic Editors: Wenyan He, Liang Zhang, Nan Li, Xue Gao, Xiangfei Zhang and Pierfranco Lattanzi

Received: 1 November 2024
Revised: 14 December 2024
Accepted: 19 December 2024
Published: 24 December 2024

Citation: Chen, S.; Xu, J.; Yang, Y.; Han, S.; Ding, P.; Song, Z.; Chen, T.; Zhang, D. Origin of the Miaoling Gold Deposit, Xiong'ershan District, China: Findings Based on the Trace Element Characteristics and Sulfur Isotope Compositions of Pyrite. *Minerals* **2025**, *15*, 6. https://doi.org/10.3390/min15010006

Copyright: © 2024 by the authors. Licensee MDPI, Basel, Switzerland. This article is an open access article distributed under the terms and conditions of the Creative Commons Attribution (CC BY) license (https://creativecommons.org/licenses/by/4.0/).

1. Introduction

The Xiong'ershan district is located on the southern boundary of the NCC and the northern edge of the Qinling Orogenic Belt (Figure 1a). Since the Archean, the region has experienced multiple phases of tectonic and magmatic activities [1–5]. Large-scale tectonic–magmatic events have not only provided sufficient energy and space for mineralization but also moved substantial amounts of mineralizing materials from deep sources. The region exhibits favorable geological conditions for mineralization, leading to the enrichment of various metals such as gold, silver, molybdenum, lead, and zinc [6–11]. Among these, gold resources are the most abundant, with more than 20 gold deposits having been discovered and a cumulative proven gold metal content exceeding 400 tons [12]. The Miaoling gold deposit can be found in the southeastern section of the Xiong'ershan district (Figure 1c). The ore body is hosted in the Mesoproterozoic Xiong'er Group of the Changcheng System of volcanic rocks [13]. It is a typical large-scale hydrothermal gold deposit for the district, with over 20 tons of proven gold reserves. Researchers have previously conducted partial studies on the sources of ore-forming materials and the evolution of ore-forming fluids, but there is still debate about these questions. It remains unclear whether the ore-forming materials were sourced from post-magmatic hydrothermal fluids that extracted them from the surrounding rocks [14–16] or whether they were supplied by deep magmatic hydrothermal fluids. Similarly, it remains unclear whether the fluids that were responsible for ore formation originated mainly from magmatic sources or from the metamorphic fluids released by subducted crust [17–19].

The main metallic mineral of the Miaoling gold deposit is pyrite, which serves as the primary gold-bearing mineral. The distribution of and variation in trace elements in pyrite can reflect the composition and physicochemical properties of the ore-forming fluids [20–23]. For example, the ratio of Co/Ni in pyrite diminishes from the initial stages to the final stages in the Sanshandao gold deposit, Jiaodong district, reflecting a continuous decrease in the mineralization temperature, which is consistent with quartz inclusion thermometry results [24]. Therefore, the variation in trace element content in pyrites from different mineralization stages can generally be utilized to reconstruct the development of fluids.

On the basis of field geological survey work, petrological and mineralogical studies were conducted on the Miaoling gold deposit. In order to gain a better understanding of the genesis of the Miaoling gold deposit, we employed a range of techniques, including LA-MC-ICP-MS for sulfur isotopes and LA-ICP-MS for trace element analyses of different generations of pyrite. These experiments provide us with more evidence to discuss the origin of the Miaoling gold deposit.

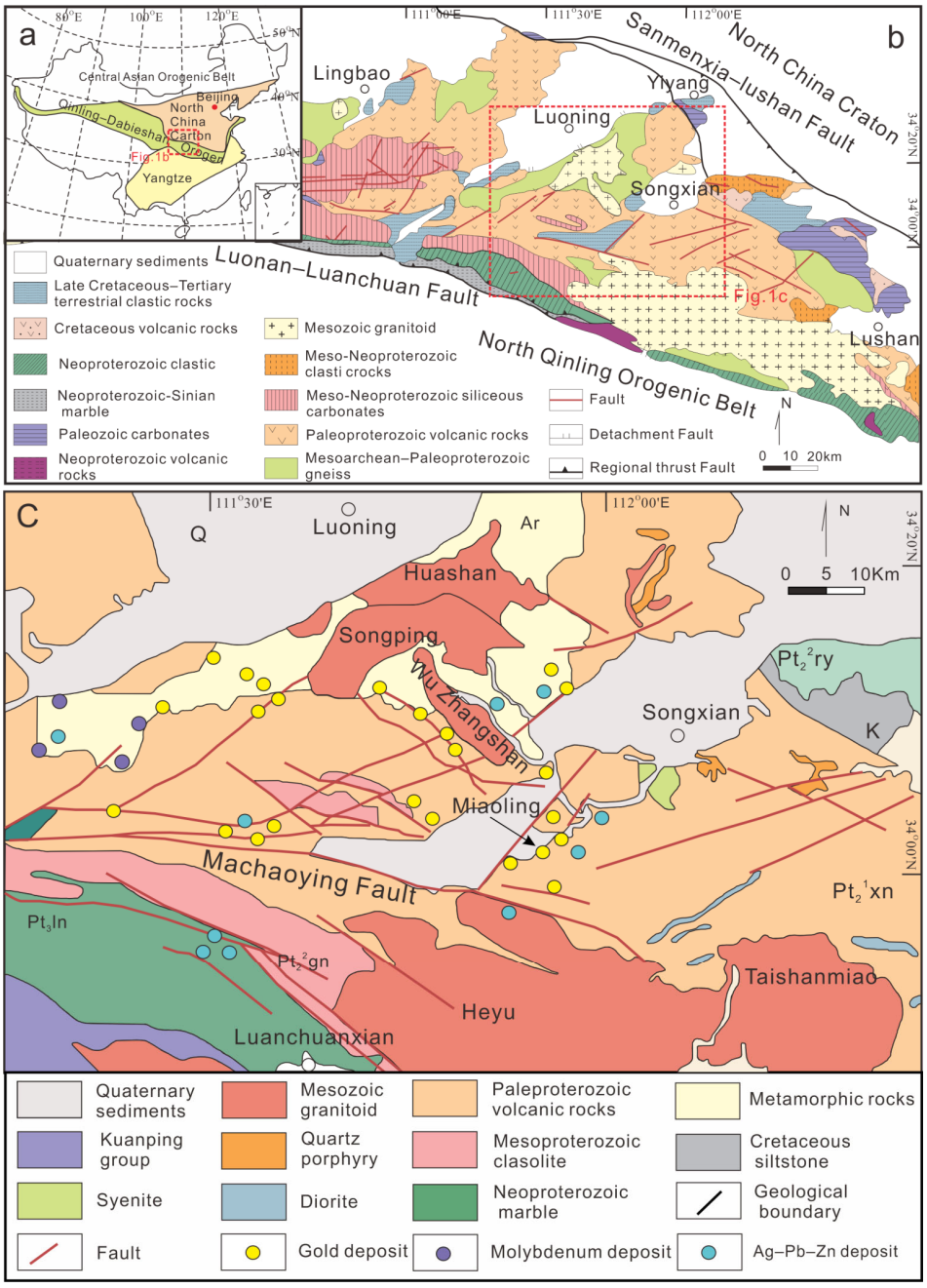

Figure 1. (**a**) Map of the distribution and locations of plates in China [25]. (**b**) Geological map of the southern margin of the NCC [5]. (**c**) Regional geological map of the Xiong'ershan district [7].

2. Regional Geology

The Xiong'ershan area is located on the southern margin of the North China Craton (NCC). The NCC is the earliest formed and largest craton in China [26], comprising the western and eastern blocks and the central orogenic belt [27]. Since the Mesoproterozoic, the NCC has entered a period of stable sedimentary cover formation, but certain regions have remained tectonically and magmatically active, such as the series of orogenic belts along the margin of the NCC, including the XingMeng Orogenic and Qinling Orogenic Belts, which formed on the periphery of the NCC during the late Paleozoic to Mesozoic. The Qinling Orogenic Belt, located in the central-eastern part of the central orogenic belt, has undergone extensive tectonic and magmatic activity since the Neoproterozoic [2,28]. By the Late Paleozoic, the complete collision and suturing of the North China and Yangtze

Plates had been achieved, marking the transition of the Qinling Orogenic Belt into a fully intracontinental orogenic stage. During the Late Triassic, lithospheric thinning occurred in this region, leading to the upwelling of asthenospheric materials [1,29]. This process created favorable conditions for subsequent large-scale metallogenic events in the area.

The geological layers in the district exhibit a typical two-layer structure: a Precambrian crystalline basement overlain by a Mesoproterozoic volcanic cover. The Precambrian crystalline basement mainly consists of Neoarchean–Paleoproterozoic Taihua Group metamorphic rocks, which are primarily composed of granitic gneiss, TTG (tonalite–trondhjemite–granodiorite) gneiss, and amphibolite. The metamorphic grade typically corresponds to amphibolite facies, with parts reaching granulite facies [30–32]. The overlying Mesoproterozoic volcanic rocks from the Xiong'er Group consist of basic, intermediate–basic, and intermediate–acidic volcanic rocks [33], including rhyolite, andesite, basaltic andesite, and rhyolitic tuff lava. These volcanic rocks unconformably overlie the Precambrian crystalline basement and represent the most significant volcanic activity in the region following the formation of the Precambrian basement [34–36].

Fold structures in the Xiong'ershan district are not prominent, with only the NE-trending Huashan–Longbo anticline and the Dazhuang–Zhonghu anticline being of significance. However, these structures are relatively simple and have little connection to the region's polymetallic mineral deposits. As a result of the impact from both the NCC and the Qinling Orogenic Belt, the district has developed fault structures. Major structures include the NE-trending Luoning fault in the north and the nearly EW-trending Machao-Ying fault in the south [37]. Additionally, a series of nearly NS-, NW-, and NE-trending secondary faults have developed in the district. These faults are considered significant ore-conducting and ore-hosting structures [5], being intimately connected to the spatial arrangement of extensive gold and polymetallic mineral deposits across the district [7,16].

Magmatic activity occurred in three main phases in this district: the Archean, Mesoproterozoic, and Mesozoic [5]. Archean magmatism primarily formed intermediate–basic to acidic volcanic rocks, which were later subjected to regional metamorphism, producing rocks such as amphibolite and granitic gneiss that constitute the crystalline basement in the district. Mesoproterozoic volcanic activity mainly produced intermediate–basic to intermediate–acidic volcanic rocks, such as andesite and rhyolite, which form the volcanic cover of the region. Mesozoic volcanic activity, mainly occurring during the Yanshanian period, was the most intense magmatic phase and was dominated by intermediate–acidic intrusive rocks. These formed porphyritic medium-coarse-grained biotite–hornblende granite, porphyritic alkali-feldspar granite, and giant porphyritic medium-coarse-grained granite. Researchers have previously suggested that the Yanshanian magmatism provided the necessary thermal conditions for the remobilization of gold, silver, and other metals from the ancient crystalline basement, making it a significant source of mineralizing materials [5,12,14,38].

3. Deposit Geology

The Miaoling gold deposit is located 89 km southwest of Luoyang city. The exposed strata in the mining district mainly belong to the Mesoproterozoic Xiong'er Group of the Changcheng System of volcanic rocks (Figure 2a). This system can be divided into the Dagushi, Xushan, Jidangping, and Majiapo Formations in ascending order. Among these, the Jidangping Formation serves as the main ore-hosting layer. The lithology of this formation is primarily composed of purplish-red rhyolite, with potassium feldspar and a small amount of quartz as the main mineral components. The fault structures are extremely developed within the mining district, trending nearly north–south and dipping westward, with dip angles ranging from 30° to 80°. The F8, F9, and F22 faults are the

main ore-controlling faults (Figure 3a). Additionally, a series of secondary faults trending east–west, northeast, and northwest are present. Ore bodies tend to be more developed at the intersections. The region has experienced intense magmatic activity, with large-scale intermediate–basic to intermediate–acidic volcanic rocks and intrusive granitic and dioritic dikes formed during Mesozoic magmatic intrusion.

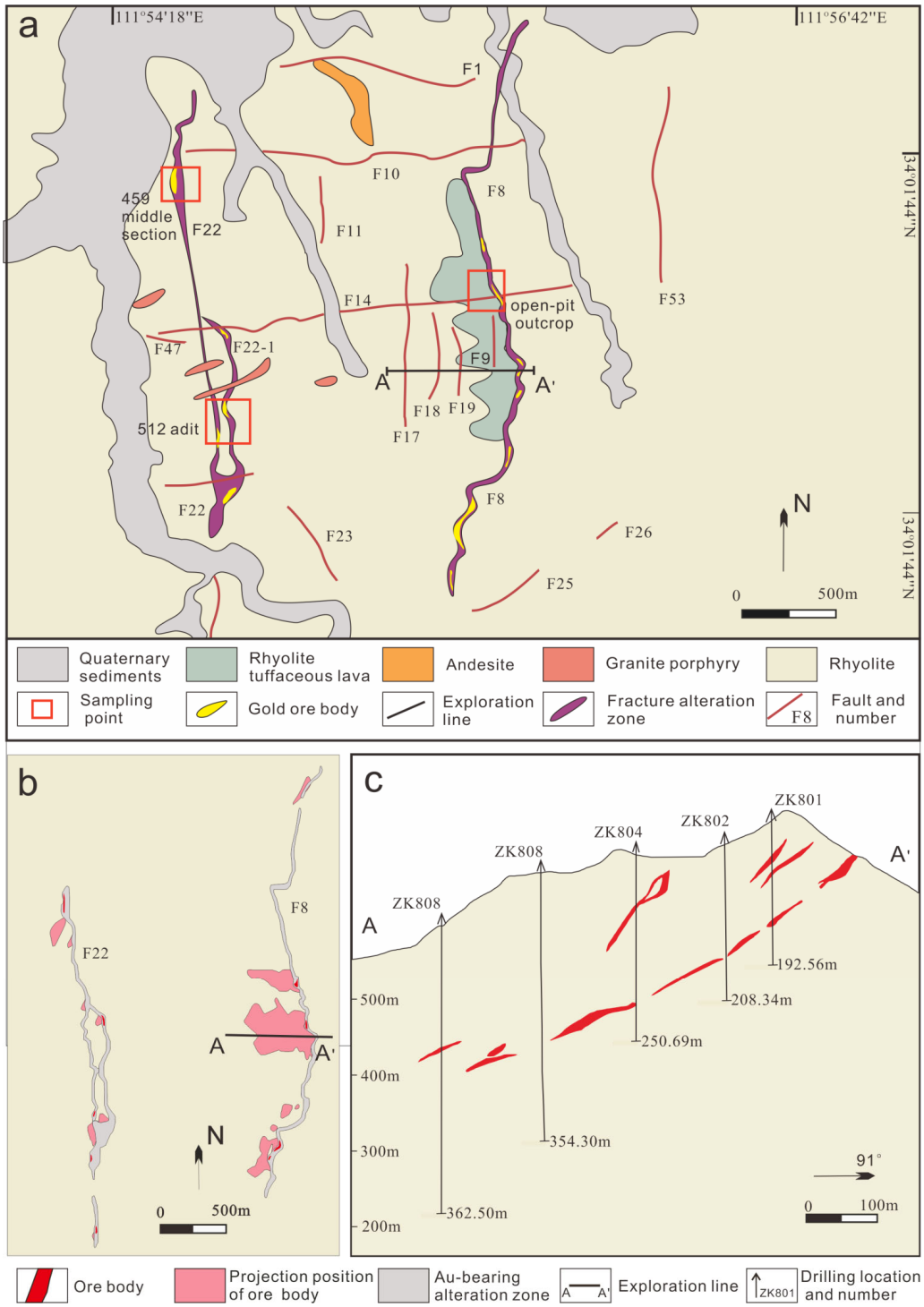

Figure 2. (**a**) Geological diagram of Miaoling gold deposit [12]. (**b**) Projection of ore body in Miaoling gold deposit [39]. (**c**) Exploration line profile of Miaoling gold deposit [40].

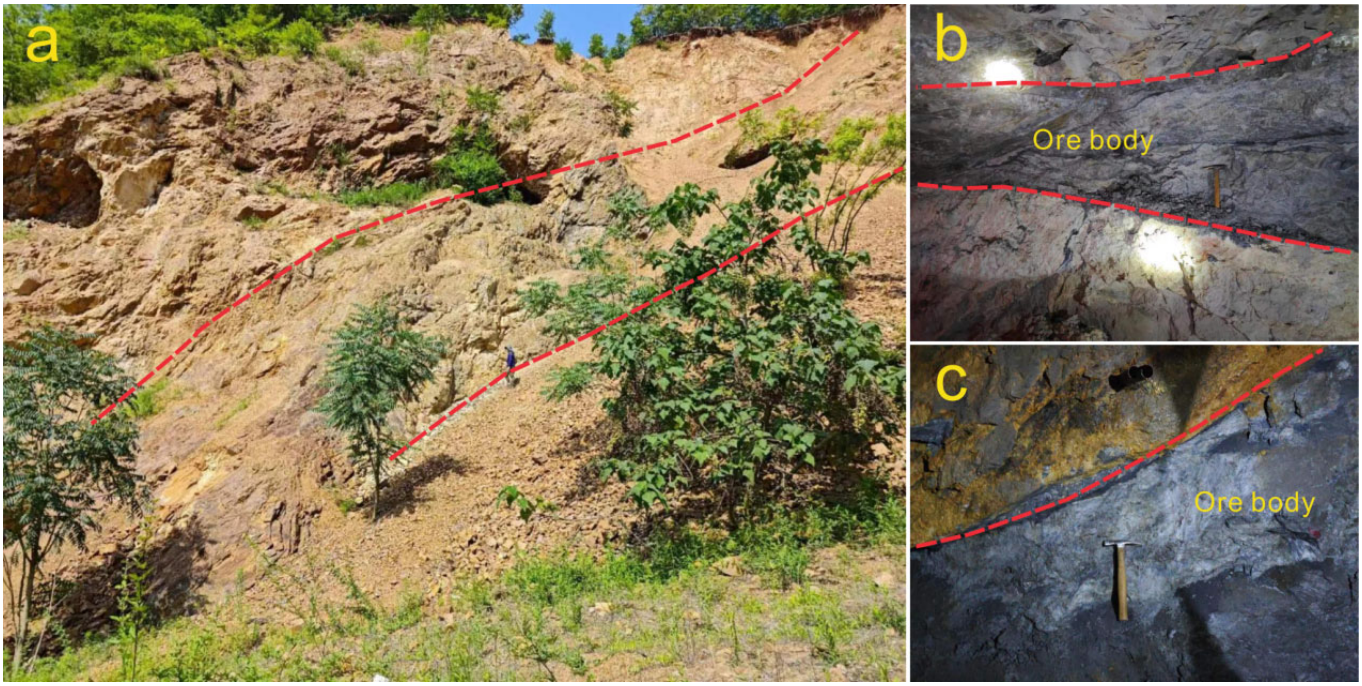

Figure 3. (**a**) F8 fault structure alteration zone. (**b**,**c**) Primary ore body in the F8 fault.

Currently, 27 gold ore bodies have been identified in the Miaoling gold deposit, distributed along the F8 (15 bodies) and F22 (12 bodies) gold-bearing fault alteration zones, with the ore bodies being strictly controlled by the fault structures (Figure 2b). Ore body no. I-3 is located in the F8 fault zone and has a vein-like, irregular large lenticular shape with good continuity. Its strike ranges from 250° to 301°, with dip angles between 19° and 56°. The thickness of its ore bodies varies between 0.44 and 13.29 m, with a gold grade between 0.21 and 70.20 g/t (with an average of 2.3 g/t; Figure 2c). Ore body no. II-2 is located in the F22 fault zone and has a vein-like and lenticular shape, tapering off as it extends southward and forming branches that pinch out. Its strike ranges from 260° to 305°, with dip angles between 45° and 82°. The thickness of the ore body is between 0.73 and 9.36 m, with a gold grade between 0.49 and 8.22 g/t (with an average of 2.2 g/t) [39].

The primary metallic minerals include pyrite, galena, and chalcopyrite (Figure 4c–e). Non-metallic minerals include quartz, potassium feldspar, sericite, calcite, and fluorite (Figure 5). The ore texture is mainly granular, with structures such as fine veinlets, disseminations, and massive forms. The main types of ore are fine disseminated and fine veinlet ores. The surrounding rock alterations include silicification, potassium feldspar alteration, sericitization, pyrite–sericite alteration, fluorite alteration, and carbonate alteration.

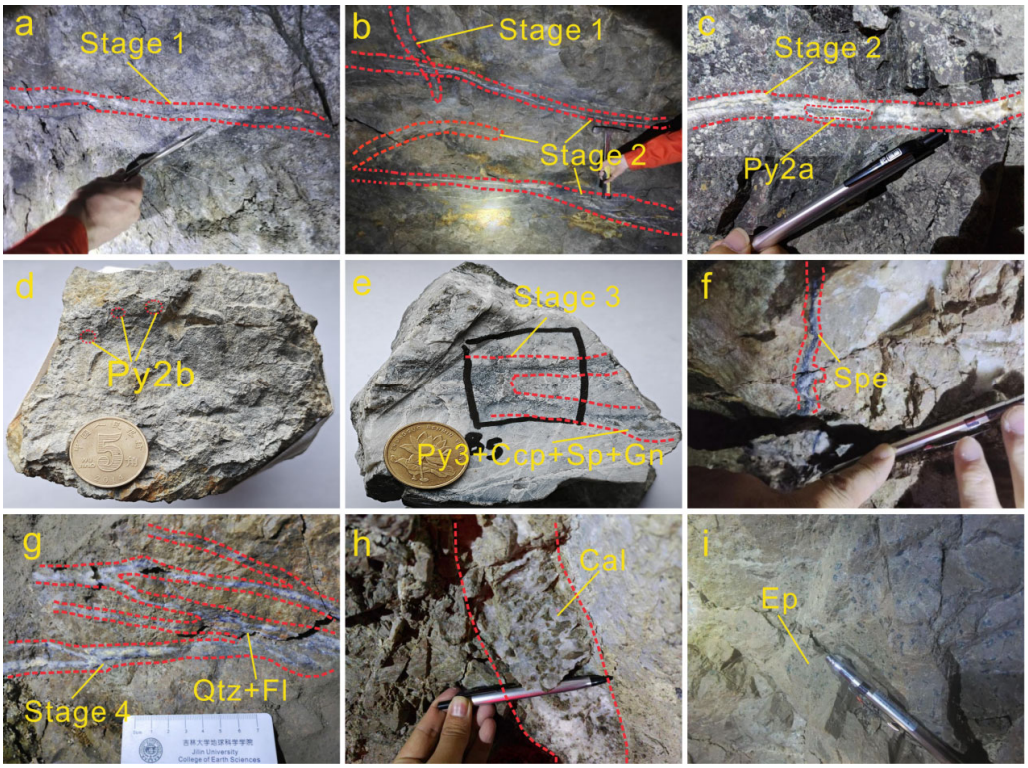

Figure 4. Field and underground photos of quartz veins and altered rocks in four stages of the Miaoling gold deposit: (**a**) Stage 1 quartz vein; (**b**) two stages of crossing–cutting quartz veins; (**c**) Stage 2 quartz vein and pyrite; (**d**) pyrite in altered rocks; (**e**) Stage 3 quartz–polymetallic sulfide vein; (**f**) specularite vein; (**g**) Stage 4 quartz–fluorite vein; (**h**) carbonate vein; (**i**) epidotization; Py—pyrite; Py2a—pyrite in quartz vein; Py2b—pyrite in altered rocks; Ccp—chalcopyrite; Sp—sphalerite; Gn—galena; Spe—specularite; Qtz—quartz; Fl—fluorite; Cal—calcite; Ep—epidotization.

Stage / Mineral	Stage1	Stage2	Stage3	Stage4
Quartz				
Potassium Felspar				
Pyrite				
Native Au				
Electrum				
Chalcopyrite				
Galena				
Sphalerite				
Sericite				
Fluorite				
Calcite				
Apatite				
Barite				
Chlorite				
Note	Max	Med	Min	

Figure 5. An overview of the paragenetic sequence from the four stages of mineralization in the Miaoling gold deposit.

Based on field observations of the veins' cross-cutting relationships, the mineralization process was categorized into four stages (Figures 4 and 5) as follows: (1) The pyrite–quartz stage (Stage 1) is characterized by weak gold mineralization, with the predominant minerals being quartz, potassium feldspar, and pyrite. The pyrite can be observed sporadically in euhedral to subhedral granular textures and displays evidence of the silicification and alteration of the potassium feldspar (Figure 4a,b). (2) The quartz–pyrite–native gold stage (Stage 2) is the primary stage of gold mineralization, and the mineral assemblage includes pyrite, quartz, potassium feldspar, fluorite, and sericite. The pyrite is mostly subhedral to anhedral, occurring as a granular and finely disseminated texture, and native gold occasionally appears (Figure 4c,d). (3) The quartz–polymetallic sulfide stage (Stage 3) is characterized by the simultaneous presence of pyrite, chalcopyrite, galena, and sphalerite. Pyrite typically occurs having an anhedral granular texture and is distributed in fine veinlets (Figure 4e). The gold mineralization is relatively strong. (4) The quartz–carbonate stage (Stage 4) is characterized by the occurrence of quartz and calcite, with gold mineralization not being observed (Figure 4g,h).

4. Sampling and Analytical Methods

4.1. Sampling and Preparation

Samples were obtained from the Miaoling gold deposit's 512-level adit, 459 middle-section project, and open-pit outcrop. A total of 14 samples from different mineralization stages were selected and subjected to in situ trace element analysis of their pyrite contents, as well as in situ sulfur isotope analysis.

4.2. In Situ Trace Element Analysis

The trace element analysis was performed at Kehui Testing (Tianjin, China) Technology Co., Ltd. (Seoul, Republic of Korea), using an Analytik Jena PQMS ICP-MS paired with a RESOLution 193 nm excimer laser ablation system. The laser beam diameter was 38 μm, with a frequency of 5 Hz and an energy density of approximately 5 J/cm². High-purity helium was used as the carrier gas. Before testing, the instrument was calibrated using NIST 610 to achieve optimal conditions. For the LA-ICP-MS laser ablation, a single-point ablation method was used. Initially, the laser beam was blocked to collect a 20-s blank signal, followed by 45 s of continuous ablation sampling, and, finally, a 20-s cleaning period to flush the system. Each single-point analysis took 85 s. Every 10 ablation points, a set of standard reference materials (NIST 610, NIST 612, BHVO-2G, BCR-2G, BIR-1G, and MASS-1) was inserted for quantitative element analysis [41]. Offline data processing (including sample and blank signal selection, instrument drift correction, and element concentration calculation) was performed using ICPMSDataCal software (ICPMSDataCal 10.2).

4.3. In Situ Sulfur Isotope Analysis

The in situ sulfur isotope analysis was also conducted at Kehui Testing (Tianjin, China) Technology Co., Ltd., using a Neptune Plus multi-collector ICP-MS from Thermo Scientific, coupled with a RESOlution SE 193 nm solid-state laser. Based on images of the samples, suitable areas were selected for the laser ablation of sulfides. Point ablation was used, with the ablation diameter being adjustable between 10 μm and 150 μm (typically 30 μm for sphalerite and chalcopyrite and 20 μm for pyrite). The energy density was 3 J/cm², with a frequency of 5 Hz. High-purity helium was used as the carrier gas to transport the aerosol produced during ablation to the MC-ICP-MS for mass spectrometry analysis. The sulfur isotopes ^{32}S and ^{34}S were simultaneously collected using Faraday cups, with an integration time of 0.131 s, collecting 200 data sets in approximately 27 s. Prior to formal analysis, the instrument parameters were adjusted using sulfide standards to reach optimal conditions.

To minimize matrix effects on the results, sulfide standards with similar matrices to the samples were used during analysis, and a standard–sample–standard bracketing method was employed for mass bias correction.

5. Results

5.1. Types of Pyrite

Based on mineralogical and petrographic studies, the pyrite was classified into three generations: Py1, Py2, and Py3. Py1 is linked to the significant development of potassium feldspar and silicification during Stage 1. Due to subsequent stress, the early potassium feldspar and silicification were fractured and later filled by hydrothermal fluids, forming silicified structural lenses. Py1 is typically medium- to fine-grained euhedral to subhedral cubic pyrite and sparsely distributed within the silicified breccia. Gold mineralization is weak (Figure 6a,b). Py2 developed during Stage 2 and can be further divided into Py2a and Py2b based on the shape and structure. Py2a is medium- to coarse-grained euhedral to subhedral cubic pyrite that developed in the mineralized quartz veins and their sides, showing strong gold mineralization (Figure 6c,d). Py2b is fine-grained and subhedral to anhedral disseminated pyrite and found in silicified, sericitized, and structurally altered rocks. It represents the stage with the strongest gold mineralization (Figure 6e,f). Py3 developed during Stage 3 and is characterized by anhedral granular and fine veinlet pyrite that is medium to fine grained; subhedral to anhedral in texture; and associated with chalcopyrite, galena, and sphalerite through inclusion, replacement, and filling structures. This stage still shows strong gold mineralization (Figure 6g).

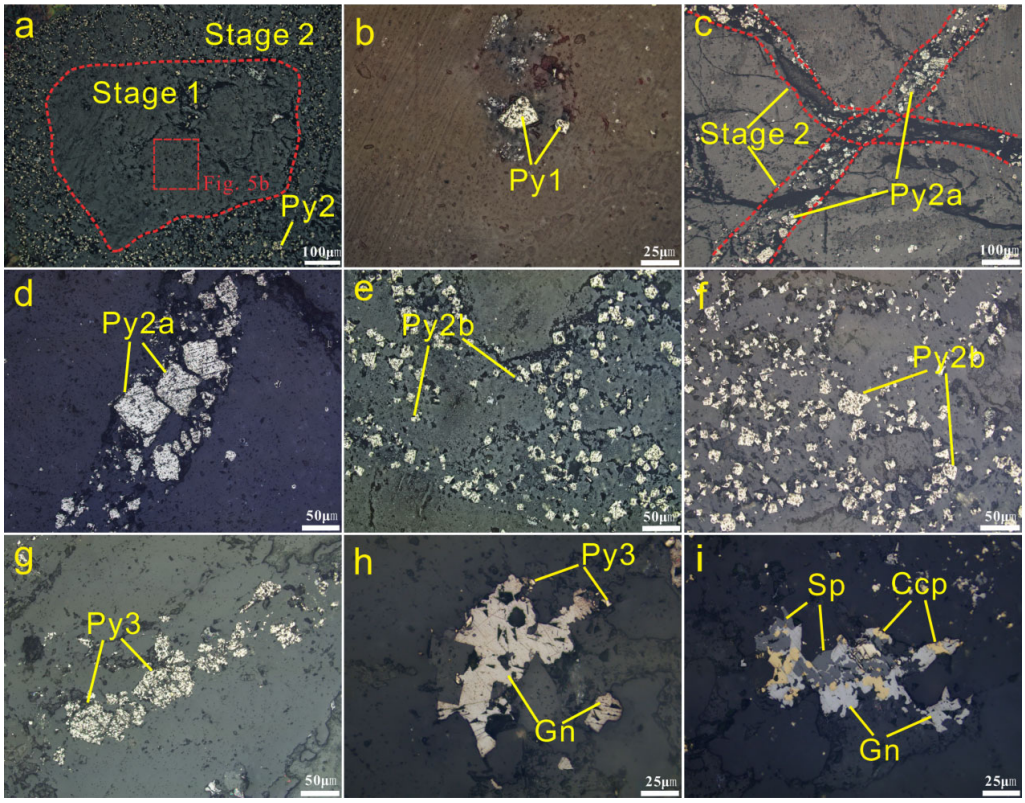

Figure 6. Microscopic photos of pyrite in Miaoling gold deposit: (**a**,**b**) pyrite in Stage 1 quartz vein; (**c**–**d**) pyrite in Stage 2 quartz vein; (**e**–**f**) pyrite in altered rocks; (g) pyrite in Stage 3 quartz vein; (**h**–**i**) polymetallic sulfide in Stage 3 quartz vein. Py—pyrite; Gn—galena; Ccp—chalcopyrite; Sp—sphalerite.

5.2. Trace Element Compositions of Pyrite

The results of the trace element analysis of the pyrite are shown in Table 1. The tested elements included Fe, Cu, Zn, As, Ag, Tl, Au, Bi, and Pb. The results indicated that the samples contained relatively high concentrations of Cu (4.04–5554.78 ppm), Pb (0.23–72051.62 ppm), Ti (1.64–10526.06 ppm), Zn (0.47–2742.6 ppm), As (16.03–17010.57 ppm), and Sb (0.73–2168.91 ppm). Additionally, various amounts of gold (Au) were detected, ranging from 0.01 to 871.47 ppm, along with Ag (0.22–357.7 ppm), Bi (0.01–414.59 ppm), and Tl (0.04–134.38 ppm). Small amounts of Sn (0.04–7.13 ppm) and In (0.01–0.4 ppm) were also found.

Table 1. LA-ICP-MS results for pyrites from the Huanxiangwa gold deposit.

Stage	Number	Au	As	Co	Ni	Cu	Pb	Zn	Ag	Te	Bi	Sb	TI
Stage 1	M2-2-1	871.47	17011	14.82	5.60	576.87	3136.5	1111.9	357.7	941.52	1.57	1325.8	134.38
Stage 2	M8-1-1	0.31	1954.	1.76	3.14	22.05	60.38	1.27	4.08	0.38	0.01	58.46	8.65
	M8-1-2	0.32	607.93	28.86	3.41	43.74	380.49	1.80	12.54	4.18	0.02	127.06	15.36
	M8-1-3	0.48	169.18	37.67	5.34	46.31	402.48	3.82	11.88	2.90	0.52	154.38	26.84
	M8-2-1	0.01	397.69	8.73	—	5.99	12.93	8.03	0.45	0.15	0.01	8.09	2.06
	M8-2-2	0.35	45.41	7.79	—	61.52	124.59	7.44	9.37	0.64	0.04	61.54	8.53
	M8-2-3	0.48	89.63	69.42	7.33	41.56	124.58	2.08	3.36	0.13	0.01	43.55	6.14
	M8-3-1	0.01	8.31	420.72	22.50	4.04	57.41	3.44	0.22	0.12	2.94	1.88	0.04
	M8-4-1	0.03	2316.4	0.43	—	6.97	0.23	0.47	—	—	0.01	4.37	0.06
	M8-5-1	0.06	76.02	5.46	4.24	11.62	35.46	2.47	1.33	—	0.01	20.22	5.29
	M8-6-1	0.72	157.31	7.47	3.24	66.12	1507.8	1.64	60.92	60.35	0.05	159.79	28.37
	M8-6-2	0.03	309.08	3.79	2.49	10.91	42.61	1.97	0.89	0.35	0.01	23.65	5.43
	M8-7-1	0.31	55.13	18.27	2.15	30.77	96.39	1.35	9.36	5.96	0.01	45.06	2.97
	M11-1-1	4.28	8568.8	17.23	6.03	5554.8	28779	1911.9	296.60	44.45	0.13	2168.9	30.31
	M11-2-1	0.55	2694.5	38.52	4.02	160.45	727.64	6.63	78.17	11.64	0.16	323.31	34.70
	M13-2-1	10.84	6330.5	12.13	4.39	1942	6382.5	665.37	171.99	36.60	0.06	1248.8	37.33
	M13-2-2	4.40	4774.7	64.03	7.21	3690.1	62020	1083.1	370.43	61.29	0.38	1979.8	19.45
	M15-1-1	1.94	3471.5	71.04	11.21	246.47	6185.5	53.81	110.33	89.71	0.08	312.18	30.27
	M15-1-2	6.84	5499.1	45.47	3.08	128.67	34404	3.38	19.20	42.02	0.49	76.91	0.89
	M15-1-3	0.18	8571.3	92.79	9.33	6.24	83.53	18.48	0.61	—	0.03	16.66	0.07
	M15-2-1	15.16	4165.5	104.70	19.40	139.51	13672	44.00	81.32	51.77	0.33	124.39	3.87
	M15-2-2	9.94	6147.9	184.16	19.68	134.26	3655.8	18.49	118.87	78.07	0.73	208.82	4.83
Stage 3	M5-1-1	0.10	16.03	198.47	3.48	287.52	28290	3.13	291.61	20.84	188.39	0.73	0.28
	M5-3-1	0.06	23.59	481.79	7.77	103.77	72052	2742.6	282.20	15.96	414.39	0.87	0.13

(—) indicates that it is below the detection limit.

In Py1, the Au content was relatively low (0.01 ppm). However, the Au content significantly increased in Py2 to between 0.01 and 871.47 ppm (with an average of 31.08 ppm). In Py3, the Au content decreased sharply to between 0.10 and 0.06 ppm (with an average of 0.08 ppm). This trend was mirrored by several other elements, such as the As content, which increased from 8.31 ppm in Py1 to 45.41–17010.57 ppm (with an average of 3072.89 ppm) in Py2 and then decreased in Py3 to 16.03–23.59 ppm (with an average of 19.81 ppm). However, the Tl content rose from 0.04 ppm in Py1 to 0.06–134.38 ppm (with an average of 16.63 ppm) in Py2 before decreasing in Py3 to 0.13–0.28 ppm (with an average of 0.20 ppm). In contrast, the trend for other elements, such as Co, was the opposite. The Co content dropped from 420.72 ppm in Py1 to 0.43–184.16 ppm (with an average of 40.32 ppm) in Py2 but then increased again in Py3 to 198.47–481.79 ppm (with an average of 340.13 ppm). Similarly, Ag and several other elements showed inverse trends. The Ag content increased from 0.22 ppm in Py1 to 0.45–357.70 ppm (with an average of 125.41 ppm) in Py2 and then rose further in Py3 to 282.20–291.61 ppm (with an average of 286.90 ppm). The Pb content grew from 57.41 ppm in Py1 to 0.23–62019.72 ppm (with an average of 5529.14 ppm) in Py2 and increased again in Py3 to 28290.37–72051.62 ppm (with an average of 50170.99 ppm) (Figure 7).

Our correlation analysis (Table 2) showed that Au is significantly positively correlated with the concentrations of elements such as As and Ag.

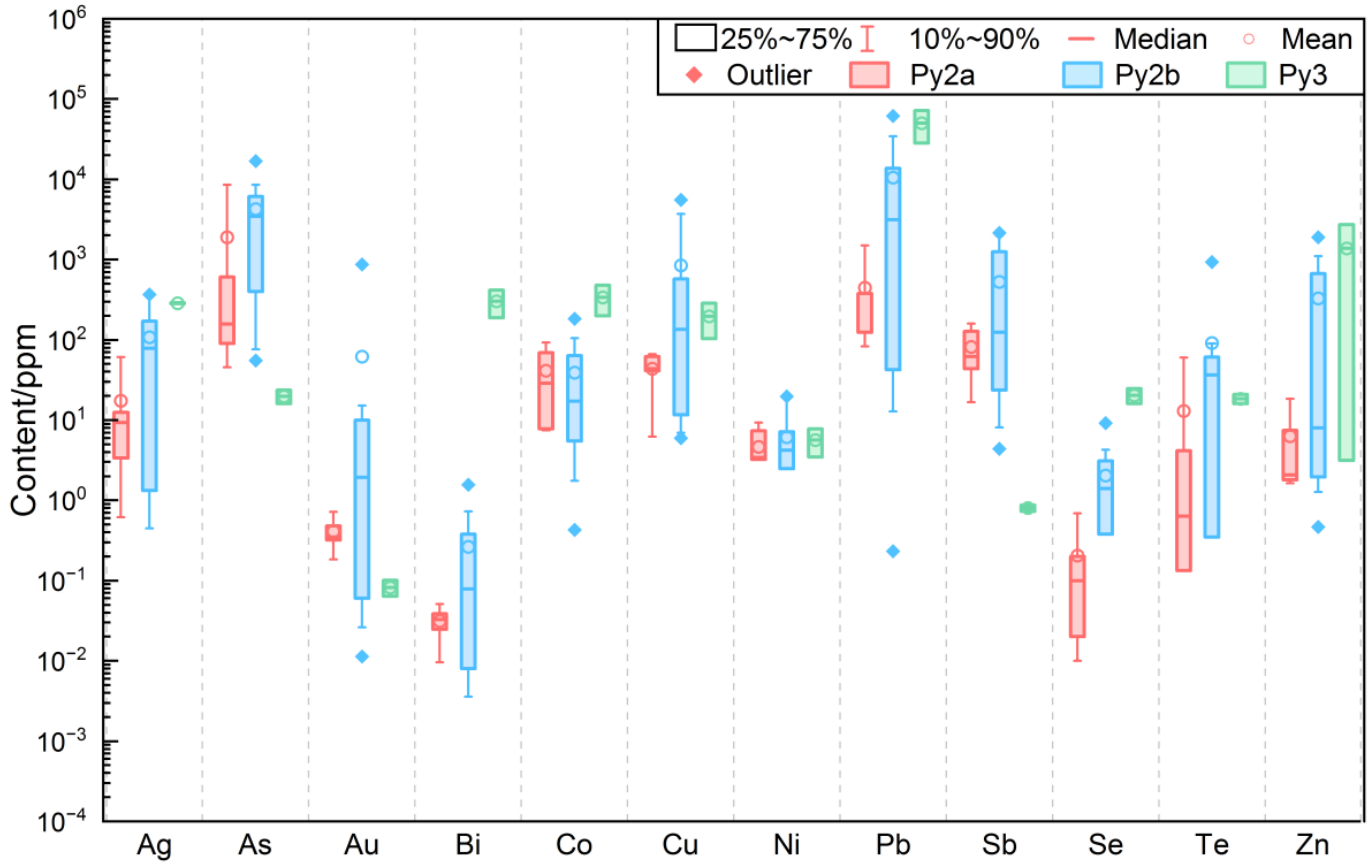

Figure 7. Box and whisker plots of trace element concentrations in pyrite, acquired by means of LA-ICP-MS analysis, from the Miaoling gold deposit.

Table 2. Correlation analysis of ore-forming elements in Miaoling gold deposit.

Element	Au	Ag	Cu	Pb	Zn	Co	Ni	As	Bi
Ag	0.44								
Cu	0.01	0.63							
Pb	−0.11	0.69	0.45						
Zn	0.24	0.74	0.56	0.75					
Co	−0.11	0.24	−0.13	0.48	0.41				
Ni	−0.02	0.08	−0.01	0.06	0.02	0.59			
As	0.73	0.52	0.39	0.07	0.33	−0.12	0.16		
Bi	−0.06	0.43	−0.08	0.68	0.63	0.71	0.01	−0.21	
TI	0.89	0.51	0.21	−0.11	0.28	−0.26	−0.08	0.73	−0.17

5.3. In Situ S Isotope Compositions of Pyrite

The test results indicated that except for Py1 (n = 1), with a positive $\delta^{34}S$ value of 4.24‰, all remaining stages exhibited significantly negative $\delta^{34}S$ values, with an average of −8.25‰ (Table 3). The $\delta^{34}S$ value of sphalerite was −8.19‰, the $\delta^{34}S$ value of chalcopyrite was −14.24‰, and the $\delta^{34}S$ value of galena was −17.9‰.

Table 3. Sulfur isotopic compositions of sulfides minerals from the Miaoling deposit.

Stage	Sulfide Generation	Sample	$\delta^{34}S$
Stage1	Py1	M8-3-1	4.24
Stage2	Py2a	M8-1-2	−9.18
	Py2a	M8-2-2	−6.63
	Py2a	M8-6-1	−8.41
	Py2a	M11-2-1	−13.79
	Py2a	M11-3-1	−13.50
	Py2b	M2-1-1	−10.52
	Py2b	M2-2-1	−9.72
	Py2b	M8-1-1	−6.63
	Py2b	M8-1-3	−9.09
	Py2b	M8-2-1	−9.03
	Py2b	M8-4-1	−8.31
	Py2b	M8-5-1	−9.50
	Py2b	M8-6-2	−7.02
	Py2b	M8-7-1	−9.39
	Py2b	M11-1-1	−12.40
	Py2b	M13-1-1	−9.60
	Py2b	M13-2-1	−10.32
	Py2b	M15-1-1	−7.94
	Py2b	M15-1-2	−9.90
	Py2b	M15-1-3	−11.39
	Py2b	M15-2-1	−11.53
	Py2b	M5-2-2	−10.75
Stage3	Py3	M5-1-1	−5.11
	Py3	M5-2-1	−5.15
	Py3	M5-3-1	−4.31
	Sp	M5-4-1	−8.19
	Gn	M5-5-1	−17.90
	Ccp	M5-6-1	−14.24

6. Discussion

6.1. Trace Element Distributions in Pyrite

In gold deposits, pyrite is the primary gold-bearing mineral and also serves as an important carrier for trace elements [20,42–44]. As the mineralization process progresses, different generations of pyrite form during different mineralization stages, and there is a significant difference in the distribution of trace elements in different generations of pyrite. Trace elements can be hosted through the following mechanisms: (1) a solid solution within the pyrite lattice; (2) nanometer-sized invisible mineral particles; and (3) micron-sized inclusions of visible sulfide, silicate, or carbonate minerals, such as native gold, chalcopyrite, galena, and sphalerite [45–51].

The LA-ICP-MS signal curves for Au are stable (Figure 8b,c), suggesting that gold mainly exists either as a solid solution or nanometer-sized particles within the pyrite lattice [52,53]. It is worth noting that anomalous peaks appear in the signal curves of Py2b and Py3 (Figure 8e,f), suggesting the presence of micron-sized gold inclusions. A significant positive correlation between Au and As (Figure 9a) indicates that gold enrichment is closely associated with arsenic [54]. Similarly, a significant positive relationship was noted between Au and Ag. (Figure 9c), with consistent signal curves (Figure 8b) accompanied by anomalous peak signals (Figure 8e). This suggests that gold and silver might exist together in the form of electrum [55]. The signal curves for Co and Ni run parallel to those for Fe (Figure 8a), indicating that Co and Ni replace Fe^{2+} [56] in the pyrite structure via isomorphism substitution. The Co content shows a positive correlation with temperature, decreasing from Py1 to Py2 and then increasing again in Py3. This suggests an initial drop in temperature followed by a rise, which is inconsistent with the overall temperature trend of the mineralizing hydrothermal system [12]. It is posited that variations in oxygen fugacity influenced the Co content, and this will be discussed in more detail below. Earlier research has shown that Pb is generally not incorporated into the pyrite lattice due to

the larger ionic radius of Pb^{2+} compared to Fe^{2+} [57]. Moreover, Pb precipitates as metal sulfides from hydrothermal fluids faster than Fe does [58]. Therefore, Pb typically exists as micron-sized mineral inclusions [53,59]. The signal curves for Pb show anomalous peaks, supporting this hypothesis (Figure 8b–d). The signal curves of the Cu and Zn in Py2b and Py3 are generally stable, with occasional anomalous peaks (Figure 8f), indicating that these elements may predominantly exist in invisible solid solutions or nanometer-sized particles, with smaller amounts being present as micron-sized mineral inclusions.

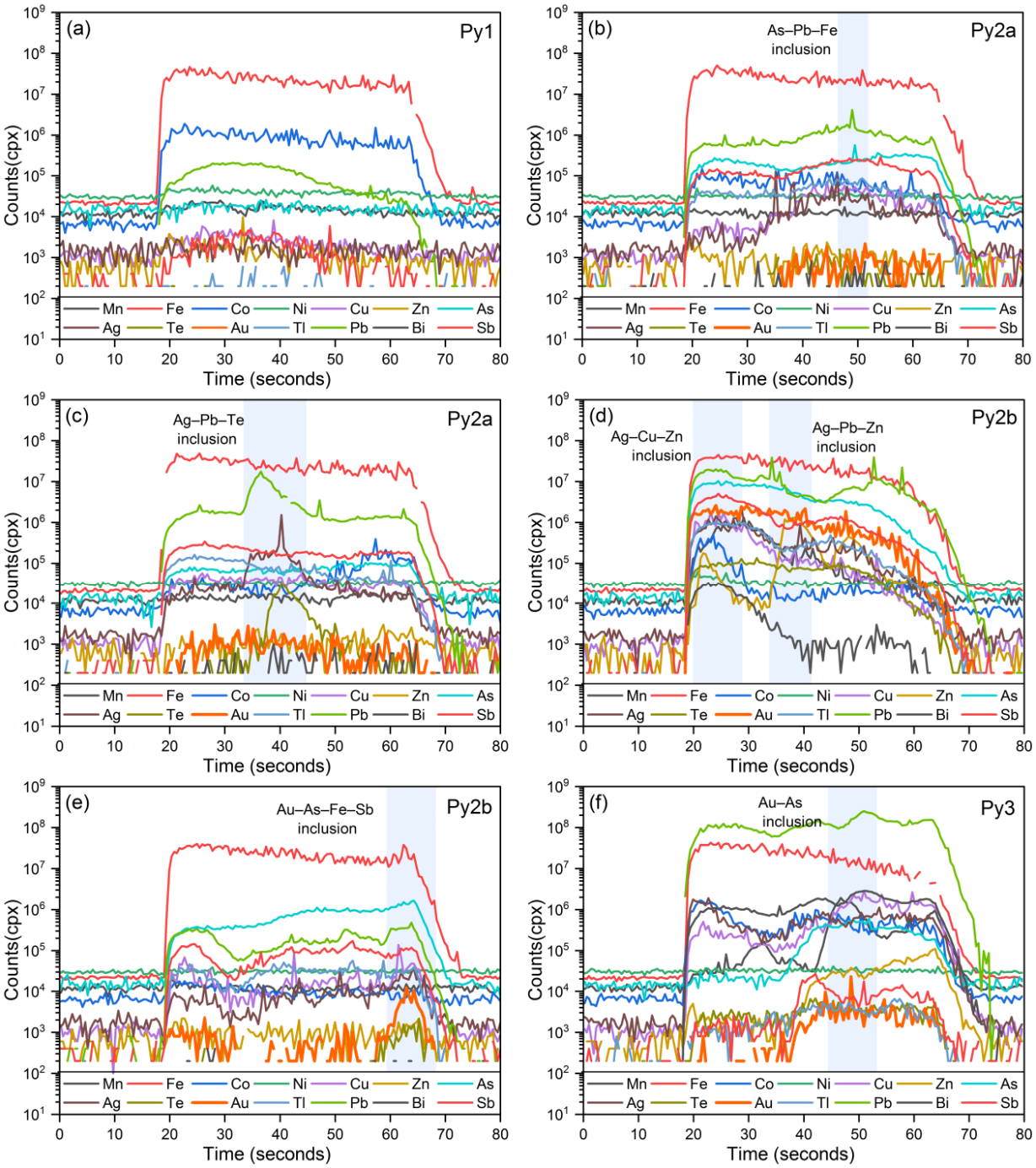

Figure 8. Graphs of LA-ICP-MS signal curves. (**a**) No gold signal was observed in Py1. (**b**–**d**) A smooth signal curve indicating the presence of gold. (**e**–**f**) Peak signal in gold data.

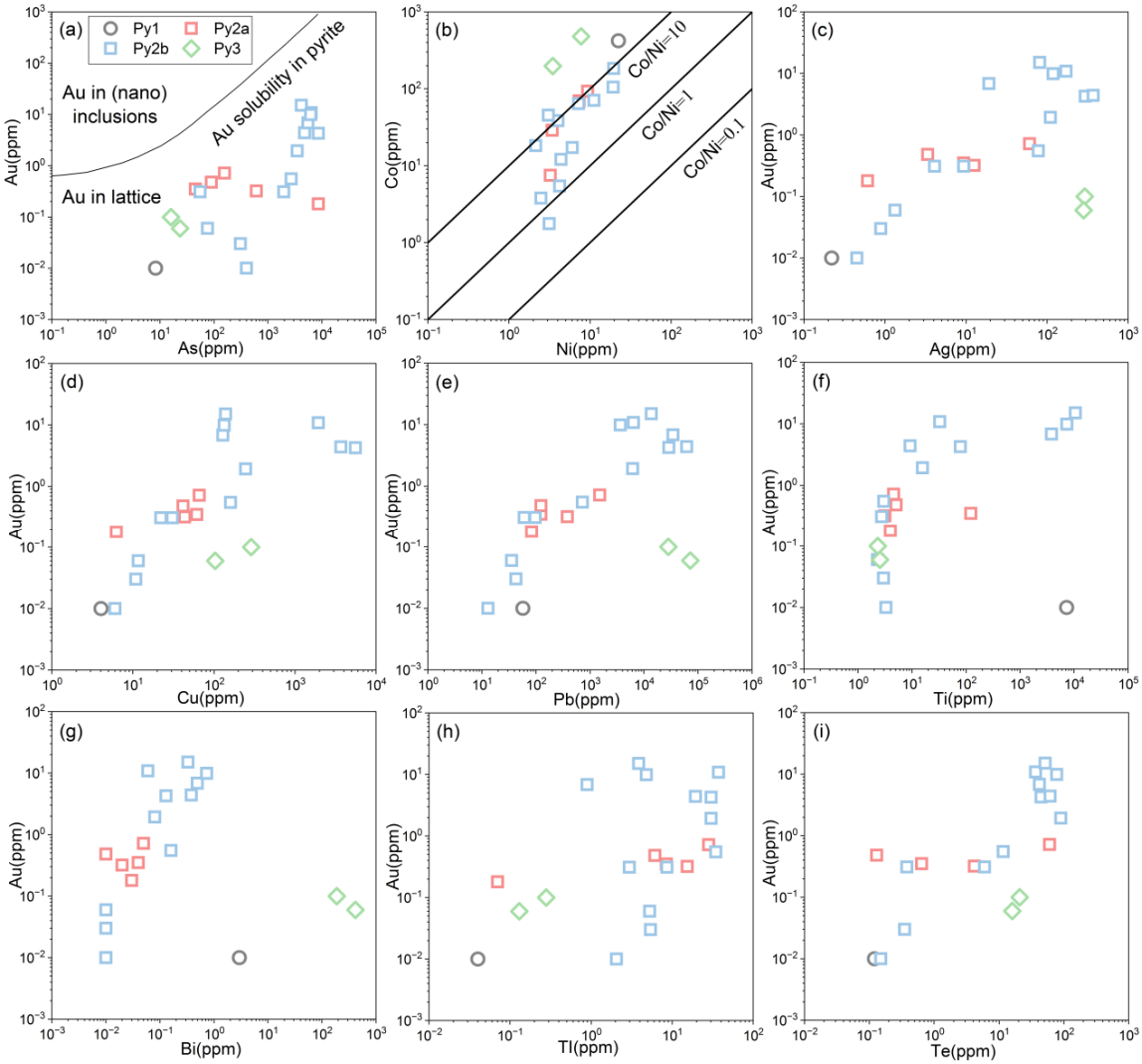

Figure 9. Binary plots of selected trace elements in the different hydrothermal stages of pyrite from the Miaoling gold deposit: (**a**) Au vs. As; (**b**) Co vs. Ni; (**c**) Au vs. Ag; (**d**) Au vs. Cu; (**e**) Au vs. Pb; (**f**) Au vs. Ti; (**g**) Au vs. Bi; (**h**) Au vs. TI; (**i**) Au vs. Te.

In summary, this study suggests that elements in the pyrite from the Miaoling gold deposit, such as Au, As, Cu, and Zn, exist both as invisible solid solutions and nanometer-sized particles, as well as micron-sized mineral inclusions. Meanwhile, Pb is typically present as micron-sized inclusions, and gold enrichment is closely related to the As content.

6.2. Gold Occurrence in Pyrite

Research indicates that gold can exist either as a solid solution within a pyrite lattice or as mineral inclusions, such as native gold, electrum, and calaverite [60–63]. Previous studies of the Miaoling gold deposit have identified the presence of native gold [12]. The LA-ICP-MS ablation signal curves for pyrite also demonstrate that gold exists both in its invisible (solid solution) and visible forms (inclusions) (Figure 8c–e). The pyrite from the main mineralization stage shows a clear positive correlation between Au and As, suggesting that the gold content and its occurrence in the Miaoling gold deposit are closely related to the arsenic concentration. This relationship exists because the ionic radius of Au^{+} is relatively large and cannot directly replace Fe^{2+} in the pyrite lattice. However, arsenic (As) can substitute Fe^{2+} as $As^{2+}/^{3+}$ (in oxidizing environments) or replace sulfur (S^{-}) as As^{-} (in reducing environments), which disrupts the pyrite lattice and allows Au^{+} to enter [54]. According to the solubility curve of Au in arsenic-bearing pyrite

($C_{Au} = 0.02 \times C_{As} + 4 \times 10^{-5}$, where C_{Au} and C_{As} are the molar fractions of Au and As, respectively) [52], the sample points measured in this study all fall below the solubility curve. This indicates that the Au concentrations in the four generations of pyrite from the Miaoling gold deposit are lower than the maximum solubility of Au in arsenic-bearing pyrite, suggesting that the invisible Au mainly exists as a solid solution (Au^+) within the pyrite lattice (Figure 9a). Additionally, the LA-ICP-MS ablation signal curves for Py2b and Py3 show anomalous peaks for Au, indicating the presence of micron-sized gold inclusions. In the binary diagrams of trace elements in pyrite, no significant correlation was observed between Au and Te (Figure 9i), indicating that the gold in the pyrite is not present in the form of tellurides [20,64]. However, the analysis of correlations showed a significant positive relationship between Au and Ag (Table 2, Figure 9c) with consistent LA-ICP-MS signal curves (Figure 9b), which are generally smooth but show occasional anomalous peaks (Figure 9e). This suggests that gold may exist in pyrite in the form of electrum (a gold–silver alloy).

In conclusion, the majority of gold occurs as a solid solution within the pyrite, whereas a minor amount exists in the form of native gold and electrum within the Miaoling gold deposit.

6.3. Fluid Evolution Based on Pyrite Compositions

Pyrite is commonly present in hydrothermal systems [65], and its trace element content and distribution can be used to infer the evolution of ore-forming fluids [65–67]. The makeup of pyrite is affected by a range of physicochemical factors [68–70]. These parameters may also be affected by processes, such as fluid boiling or mixing, making pyrite trace elements useful in reconstructing the evolution of ore-forming fluids [71].

The contents of Co and Ni in pyrite reflect changes in the temperature within hydrothermal systems [72]. The solubility of the cobalt chloride complex $CoCl_4^{2-}$ in hydrothermal systems is strongly correlated with the temperature [73,74]. Specifically, a decrease in temperature from 300 °C to 200 °C can reduce the solubility of Co by two orders of magnitude [75]. The Co content in pyrite decreases from Py1 (420.72 ppm) to Py2 (0.43–184.16 ppm, with an average of 40.32 ppm) and then increases again in Py3 (198.47–481.79 ppm, with an average of 340.13 ppm) (Figure 7). This suggests a trend in which the hydrothermal temperature first decreased and then increased, although this contradicts the fluid inclusion temperature measurements that show a steady decline from Py1 (205–341 °C, with an average of 268 °C) to Py2 (161–257 °C, with an average of 201 °C) and Py3 (143–225 °C, with an average of 192 °C) [12]. Thus, we inferred that the temperature had little influence on the Co content in this deposit.

The solubility of Bi is affected by oxygen fugacity, showing a negative correlation [76]. In the Miaoling gold deposit, the Bi content decreased from Py1 (2.94 ppm) to Py2 (0.01–1.57 ppm, with an average of 0.15 ppm) and then rose in Py3 (188.39–414.59 ppm, with an average of 301.49 ppm), indicating that the oxygen fugacity initially increased from Py1 to Py2, followed by a subsequent decrease from Py2 to Py3, which is consistent with the trend observed for Co. Therefore, we suggest that the contents of Co, Bi, and similar elements were primarily controlled by changes in oxygen fugacity, with an increase from Py1 to Py2 and a decrease from Py2 to Py3.

The As content in pyrite is affected by the fluid temperature and the rate of pyrite crystallization. Lower temperatures and rapid crystallization can lead to arsenic enrichment [77,78]. In the Miaoling gold deposit, the As content rose from Py1 (8.31 ppm) to Py2 (45.41–17010.57 ppm, with an average of 3073.03 ppm) and then declined in Py3 (16.03–23.59 ppm, with an average of 19.81 ppm), a trend that does not align with the temperature decrease indicated by a previous study on fluid inclusion. The fine-grained

subhedral–anhedral pyrite that formed in Py2 is the result of rapid crystallization, which may explain the higher As content during this stage.

6.4. Source of Ore-Forming Materials and Deposit Genesis

The sulfur isotope composition of ore minerals has been widely used to investigate sources of ore-forming materials. In systems with simple mineral assemblages and a lack of sulfate minerals, the $\delta^{34}S$ values of sulfides can approximately represent the total sulfur isotope composition of the hydrothermal fluid [79–83]. In the Miaoling gold deposit, the main ore minerals are composed of pyrite, chalcopyrite, galena, and sphalerite. Additionally, previous studies have identified sulfate minerals, such as barite [12], indicating that the $\delta^{34}S$ values of sulfides may not fully reflect the overall sulfur isotope composition.

The analysis results showed that the pyrites from the early mineralization stage had a $\delta^{34}S$ value of 4.24‰, while the $\delta^{34}S$ values during the main mineralization stage were significantly negative (−13.79‰ to −4.31‰, with an average of −9.65‰). This suggests that the hydrothermal fluids could have obtained sulfur from different sources. The surrounding rocks (the Mesoproterozoic Xiong'er Group of the Changcheng System of volcanic rocks) in the Miaoling deposit had positive $\delta^{34}S$ (2.5~5.4‰, with an average of 4.2‰) [84] (Figure 10), indicating that the sulfur in the pyrite did not source elements from the surrounding rocks. Two main reasons may explain the negative $\delta^{34}S$ values: (1) the initial sulfur in the ore-forming materials had negative $\delta^{34}S$ values, as is common with biologically derived ($\delta^{34}S$ = −40‰ to 20‰) and sedimentary ($\delta^{34}S$ = −50‰ to 50‰) sulfur; or (2) throughout the mineralization process, alterations in the mineralizing environment may induce sulfur isotope fractionation, resulting in negative $\delta^{34}S$ values. Previous studies suggest that the addition of sulfur from the surrounding strata contributed to the more negative $\delta^{34}S$ values. In the southern Xiong'ershan district, the carbonate and clastic rocks of the Guandaokou Group may have undergone metamorphism during subduction in the Mesoproterozoic due to the influence of Yanshanian magmatic activity, releasing volatile substances and providing sulfur for mineralization [85,86]. However, it has been noted that these strata are sulfur poor, and metamorphic degassing alone would not provide enough sulfur to account for the many gold deposits [5]. Additionally, no evidence of biogenic or organic sulfur has been found in the surrounding rocks of the Miaoling gold deposit. Therefore, the negative $\delta^{34}S$ values in the pyrite are likely unrelated to the sulfur from the surrounding strata.

The sulfur isotope composition of sulfides in hydrothermal deposits is influenced by the total sulfur isotope composition of the fluid ($\delta^{34}S_{\sum}$), temperature (T), oxygen fugacity ($f(O_2)$), pH, and Eh [87]. Earlier research on fluid inclusion indicates that the mineralization temperatures ranged from 341 to 101 °C, with pH values of 5.60 to 7.13 and Eh values of −0.40 to −0.12 [12]. At low oxygen fugacity, sulfur exists primarily as S^{2-} and HS^{-}. As the oxygen fugacity increases, sulfur isotope fractionation occurs, producing SO_4^{2-} that is enriched in ^{34}S. The precipitation of SO_4^{2-} depletes the remaining hydrothermal fluid of ^{34}S, causing sulfides to exhibit negative $\delta^{34}S$ values. The observed Bi content in the pyrite decreased from Py1 to Py2 and then increased in Py3, suggesting a higher degree of oxygen fugacity throughout the primary mineralization phase. The presence of barite further supports the idea that the hydrothermal fluid had a relatively high degree of oxygen fugacity during this stage. Therefore, we assert that sulfur isotope fractionation, driven by increasing oxygen fugacity, is the primary reason for the strongly negative $\delta^{34}S$ values in sulfides from the Miaoling gold deposit. Calculations based on the $\delta^{34}S$ values of sulfides and sulfate in the hydrothermal system suggest that the $\delta^{34}S_{\sum}$ value during the main mineralization stage ranged from 0.31‰ to 2.68‰ (Figure 10b) [87,88], which is consistent

with typical magmatic sulfur values ($\delta^{34}S$ ranging from −3‰ to 7‰) [89,90]. This indicates that the ore-forming materials likely originated from magmatic hydrothermal fluids.

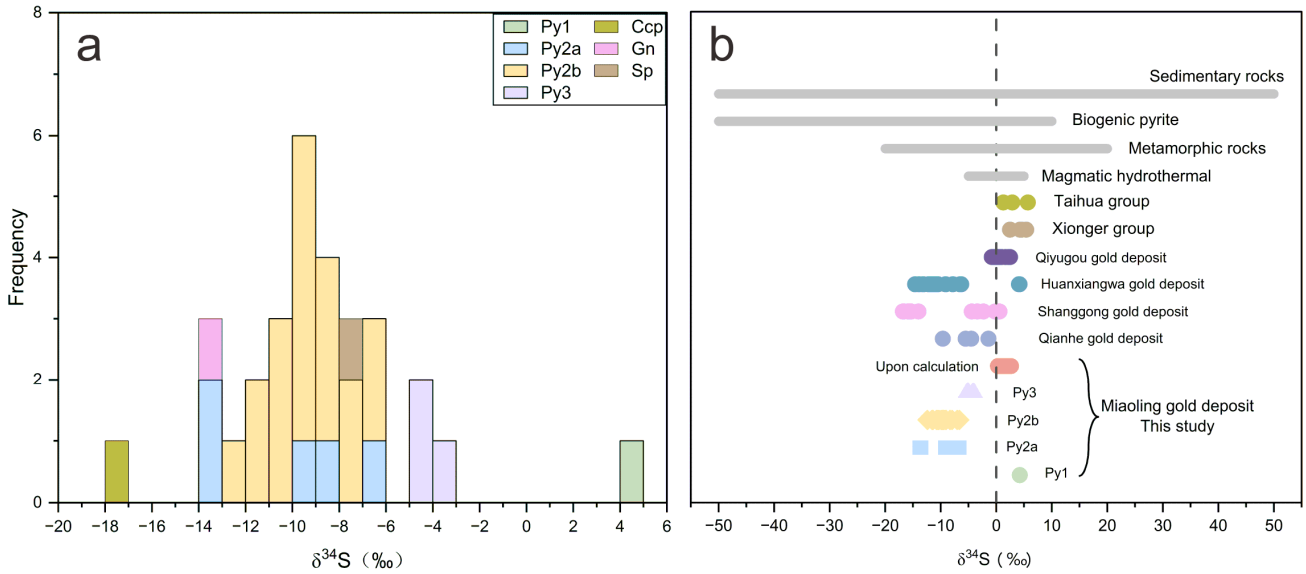

Figure 10. (**a**) A histogram of the sulfur isotopic compositions of sulfides from the Miaoling gold deposit. (**b**) The ranges of $\delta^{34}S$ values in the Miaoling gold deposit and other deposits [5,12,84,87,88,91].

Pyrite is the main gold-bearing mineral in gold deposits, and its trace element composition and the ratios between these elements provide important insights into the sources of ore-forming materials and the genesis of a deposit [65]. Co and Ni in pyrite substitute for Fe through isomorphism, and the Co/Ni ratio is widely used to distinguish between different genetic types of pyrite [92]. Pyrite with a Co/Ni ratio of less than 1 is typically considered sedimentary, whereas pyrite with a Co/Ni ratio greater than 1, particularly in the range of 1 to 5, is generally of a hydrothermal origin [93]. Co/Ni ratios between 0.56 and 62.02 (with an average of 12.34), with most values being greater than 1 and concentrated between 1 and 10 (Figure 9b), indicate typical hydrothermal pyrite characteristics.

By comparing the mineral composition, ore characteristics, and surrounding rock alterations with representative hydrothermal gold deposits in the district (Table 4), it can be found that the Miaoling gold deposit and the hydrothermal gold deposit have significant similarities in terms of their deposit characteristics.

In conclusion, we assert that the Miaoling gold deposit is a hydrothermal gold deposit that was formed during the Yanshanian period in the context of the destruction of the NCC. The main supporting evidence includes the following: (1) the ore bodies are hosted within tectonic alteration zones (Figure 3), with an ore body occurrence that is consistent with the orientations of fault structures; (2) alterations in the surrounding rocks include potassium feldspar alteration, silicification, sericitization, pyrite–sericite alteration, chloritization, epidotization, fluorite alteration, and carbonate alteration (Figure 6); (3) the mineral assemblage includes pyrite, chalcopyrite, galena, and sphalerite (Figure 4); (4) the $\delta^{34}S\sum$ values of the hydrothermal fluids during the main mineralization stage range from 0.31‰ to 2.68‰, and the Co/Ni ratios in the pyrite range from 0.56 to 62.02 (with an average of 12.34), indicating that the ore-forming materials likely originated from magmatic hydrothermal fluids; and (5) the characteristics of the Miaoling gold deposit are consistent with typical hydrothermal gold deposits in the district (Table 4).

Table 4. Geological characteristics of Miaoling gold deposit and comparison with typical hydrothermal gold deposits [5,12,40,91].

Deposit Characteristics	Miaoling	Qianhe	Gongyu	Shanggong
Ore-hosting layer	Jidangping Formation of the Xiong'er Group	Jidangping Formation of the Xiong'er Group	Xushan Formation of the Xiong'er Group	Xushan Formation of the Xiong'er Group
Ore type	Tectonically altered rock	Tectonically altered rock	Tectonically altered rock	Tectonically altered rock, explosion breccia
Mineral combination	Pyrite, sphalerite, galena, chalcopyrite, electrum and quartz, potassium feldspar, calcite, and fluorite	Pyrite, sphalerite, galena, chalcopyrite, molybdenite, native gold, electrum and quartz, potassium feldspar, and calcite	Pyrite, sphalerite, galena, chalcopyrite, limonite, scheelite, argentite and quartz, potassium feldspar, calcite, and biotite	Pyrite, sphalerite, galena, chalcopyrite, scheelite, calaverite and quartz, calcite, chlorite, sericite, and fluorite
Gold-bearing mineral	Pyrite	Pyrite	Pyrite	Pyrite
Ore-controlling structure	Near north–south fault	Near east–west fault	Northeast fault	Northeast fault
Surrounding rock alterations	Silicification, potassium feldspar alteration, sericitization, pyrite–sericite alteration, fluorite alteration, and carbonate alteration	Silicification, potassium feldspar alteration, sericitization, pyrite–sericite alteration, chloritization, and epidotization	Silicification, potassium feldspar alteration, sericitization, Epidotization, and carbonate alteration	Silicification, potassium feldspar alteration, sericitization, pyrite–sericite alteration, fluorite alteration, carbonate alteration, and chloritization
$\delta^{34}S$	−13.79–0.24‰ Average of −8.65‰	−10.60–0.26‰ Average of −4.28‰	−1.9–1.1‰ Average of −0.15‰	−14.3—13.3‰ Average of −13.75‰
Mineralization age	127–121 Ma	127–123 Ma	130–124 Ma	236–227 Ma

7. Conclusions

1. The pyrite in the Miaoling gold deposit can be divided into four generations (Py1, Py2a, Py2b, and Py3). The trace element characteristics of the pyrite indicate that the Au content in the ore-forming fluid is closely related to As.
2. Gold mainly exists in the form of a solid solution within the pyrite lattice, with smaller amounts being present as mineral inclusions of native gold and electrum.
3. During the main mineralization stages (Py2 and Py3), the $\delta^{34}S_{\Sigma}$ values (0.31–2.68‰) and Co/Ni ratios (0.56–62.02, with an average of 12.34) of the pyrite suggest that the ore-forming materials likely originated from magmatic hydrothermal fluids, confirming the deposit as a hydrothermal gold deposit.

Author Contributions: Conceptualization, S.C., Z.S. and T.C.; investigation, Y.Y., P.D. and D.Z.; resources, Y.Y. and J.X.; writing—original draft preparation, S.C.; writing—review and editing, S.H. and T.C.; project administration, Y.Y. All authors have read and agreed to the published version of the manuscript.

Funding: This research was supported by China Geological Survey (DD20190159).

Data Availability Statement: Data are contained within the article.

Acknowledgments: We would like to express our gratitude to the teachers and classmates who provided me with assistance during the writing process, as well as the relevant personnel from the First Geological and Mineral Exploration Institute of Henan Province, for their help in on-site and underground tunnel investigations.

Conflicts of Interest: Junqiang Xu and Peichao Ding are employed Company HeNan First Geology and Mineral Survey Institute. Zhaoyang Song are employed Company Seventh Geological Brigade, Hubei Geological Bureau.The paper reflects the views of the scientists and not the companies.

References

1. Yang, J.H.; Sun, J.F.; Chen, F.; Wilde, S.A.; Wu, F.Y. Sources and Petrogenesis of Late Triassic Dolerite Dikes in the Liaodong Peninsula: Implications for Post-Collisional Lithosphere Thinning of the Eastern North China Craton. *J. Petrol.* **2007**, *48*, 1973–1997. [CrossRef]
2. Dong, Y.P.; Zhang, G.W.; Neubauer, F.; Liu, X.M.; Genser, J.; Hauzenberger, C. Tectonic Evolution of the Qinling Orogen, China: Review and Synthesis. *J. Asian Earth Sci.* **2011**, *41*, 213–237. [CrossRef]

3. Zhai, L.; Ye, H.S.; Zhou, K.; Meng, F.; Gao, Y.L. Geological Characteristics and K-Feldspar 40ar/39ar Dating of the Miaoling Gold Deposit in Songxian County, Henan Province. *Geol. Bull. China* **2012**, *31*, 569–576.
4. Zhai, M.G. Tectonic Evolution and Metallogenesis of North China Craton. *Miner. Depos.* **2010**, *29*, 24–36. [CrossRef]
5. Tang, K.F. Characteristics, Genesis, and Geodynamic Setting of Representative Gold Deposits in the Xiong'ershan District. *South. Margin* North China Craton. Ph.D. Dissertation, China University of Geosciences, Wuhan, China, 2014.
6. Mao, J.W.; Xie, G.Q.; Bierlein, F.; Qü, W.J.; Du, A.D.; Ye, H.S.; Pirajno, F.; Li, H.M.; Guo, B.J.; Li, Y.F.; et al. Tectonic Implications from Re-Os Dating of Mesozoic Molybdenum Deposits in the East Qinling-Dabie Orogenic Belt. *Geochim. Cosmochim. Acta* **2008**, *72*, 4607–4626. [CrossRef]
7. Zhang, Z.; Zeng, Q.; Guo, Y.; Wang, R.; Yang, J.; Chen, Y. Genesis of the Kangshan Au-Polymetallic Deposit, Xiong'ershan District, North China Craton: Constraints from Fluid Inclusions and C-H-O-S-Pb Isotopes. *Ore. Geol. Rev.* **2020**, *127*, 103815. [CrossRef]
8. Zhai, M.; Santosh, M. Metallogeny of the North China Craton: Link with Secular Changes in the Evolving Earth. *Gondwana Res.* **2013**, *24*, 275–297. [CrossRef]
9. Bao, Z.W.; Zeng, Q.S.; Zhao, T.P.; Yuan, Z.L. Geochemistry and Petrogenesis of the Ore-Related Nannihu and Shangfanggou Granite Porphyries from East Qinling Belt and Their Constaints on the Molybdenum Mineralization. *Acta Petrol. Sin.* **2009**, *25*, 2523–2536.
10. Mao, J.W.; Zheng, R.F.; Ye, H.S.; Gao, J.J.; Chen, W. 40ar/39ar Dating of Fuchsite and Sericite from Altered Rocks Close to Ore Veins in Shagou Large-Size Ag-Pb-Zn Deposit of Xiong'ershan Area, Western Henan Province, and Its Significance. *Miner. Depos.* **2006**, *4*, 359–368.
11. Zheng, R.F.; MAO, J.W.; Gao, J.J. Characteristics of Sulfide and Silver Minerals in Shagou Silver-Lead-Zinc Deposit of Xiong'er Shan, Henan Province, and Their Significance. *Miner. Depos.* **2006**, *6*, 715–726.
12. Li, Z.Y. Geological Characteristics and Metallogenesis in the Miaoling Gold Deposit, Western Henan Province, China University of Geosciences. Master's Thesis, China University of Geosciences, Beijing, China, 2015.
13. Cao, Y.; Li, S.R.; Shen, J.F.; Yao, M.J.; Li, Q.K.; Mao, F.L. Fluid-Rock Interaction in Ore-Forming Process of Qianhe Structure-Controlled Alteration-Type Gold Deposit in Western Henan Province. *Miner. Depos.* **2008**, *27*, 714–726.
14. Fan, H.R.; Xie, Y.H.; Wang, Y.L. Fluid-Rock Interaction During Mineralization of the Shanggong Structure-Controlled Alteration-Type Gold Deposit in Western Henan Province, Central China. *Acta Petrol. Sin.* **1998**, *14*, 529–541.
15. Zhang, Z.M.; Zeng, Q.D.; Wang, Y.B.; Guo, Y.P.; Yu, B.; Wang, R.L.; Yang, J.H.; Chen, Y.K. Metallogenic Age and Fluid Evolution of the Kangshan Au-Polymetallic Deposit in the Southern Margin of the North China Craton:Constraints from Monazite U-Pb Age, and in-Situ Trace Elements and S Isotopes of Pyrite. *Acta Petrol. Sin.* **2023**, *39*, 865–885. [CrossRef]
16. Qi, D.M.; Zhou, H.W.; Gong, Y.J.; Xiong, S.F.; Jia, D.; Zhang, J.; Zhang, M.Y. Element Mobility During the Fluid-Rock Hydrothermal Alteration: Evidence from Altered Porphyritic Granite in IV Pipe of the Qiyugou Gold Deposit, Henan Province. *Acta Petrol. Sin.* **2015**, *31*, 2655–2673.
17. Liu, Y.W. The Geological Characteristics of Miaoling Gold Deposit and Its Ore-Finding Orientation. *Gold* **2003**, *4*, 19–21.
18. Yang, J.H.; Wu, F.Y.; Wilde, S.A. A Review of the Geodynamic Setting of Large-Scale Late Mesozoic Gold Mineralization in the North China Craton: An Association with Lithospheric Thinning. *Ore Geol. Rev.* **2003**, *23*, 125–152. [CrossRef]
19. Han, Y.G.; Zhang, S.H.; Franco, P.; Zhang, Y.H. Evolution of the Mesozoic Granites in the Xiong'ershan-Waifangshan Region, Western Henan Province, China, and Its Tectonic Implications. *Acta Geol. Sin. Engl. Ed.* **2007**, *81*, 253–265.
20. Chen, Y.J.; Pirajno, F.; Qi, J.P. The Shanggong Gold Deposit, Eastern Qinling Orogen, China: Isotope Geochemistry and Implications for Ore Genesis. *J. Asian Earth Sci.* **2008**, *33*, 252–266. [CrossRef]
21. Chen, Y.J.; Pirajno, F.; Li, N.; Guo, D.S.; Lai, Y. Isotope Systematics and Fluid Inclusion Studies of the Qiyugou Breccia Pipe-Hosted Gold Deposit, Qinling Orogen, Henan Province, China: Implications for Ore Genesis. *Ore Geol. Rev.* **2009**, *35*, 245–261. [CrossRef]
22. Mao, J.W.; Li, Y.Q.; Goldfarb, R.; He, Y.; Zaw, K. Fluid Inclusion and Noble Gas Studies of the Dongping Gold Deposit, Hebei Province, China: A Mantle Connection for Mineralization? *Econ. Geol. Bull. Soc. Econ. Geol.* **2003**, *98*, 517–534. [CrossRef]
23. Fan, H.R.; Hu, F.F.; Wilde, S.A.; Yang, K.F.; Jin, C.W. The Qiyugou Gold-Bearing Breccia Pipes, Xiong'ershan Region, Central China: Fluid-Inclusion and Stable-Isotope Evidence for an Origin from Magmatic Fluids. *Int. Geol. Rev.* **2011**, *53*, 25–45. [CrossRef]
24. Cook, N.J.; Ciobanu, C.L.; Mao, J.W. Textural Control on Gold Distribution in as-Free Pyrite from the Dongping, Huangtuliang and Hougou Gold Deposits, North China Craton (Hebei Province, China). *Chem. Geol.* **2009**, *264*, 101–121. [CrossRef]
25. Wang, P.; Mao, J.; Ye, H.; Jian, W.; Chen, X.; Tian, Y.; He, S.; Yan, J.; Wu, S.; Wan, L. The Qiyugou Au Orefield—An Intrusion-Related Gold System in the Eastern Qinling Ore Belt, China: Constraints from Sims Zircon U-Pb, Molybdenite Re-Os, Sericite 40ar-39ar Geochronology, in-Situ S-Pb Isotopes, and Mineralogy. *Ore Geol. Rev.* **2020**, *124*, 103636. [CrossRef]
26. Landtwing, M.R.; Pettke, T.; Halter, W.E.; Heinrich, C.A.; Redmond, P.B.; Einaudi, M.T.; Kunze, K. Copper Deposition During Quartz Dissolution by Cooling Magmatic-Hydrothermal Fluids: The Bingham Porphyry. *Earth Planet. Sci. Lett.* **2005**, *235*, 229–243. [CrossRef]

27. Williams-Jones, A.E.; Migdisov, A.A. Experimental Constraints on the Transport and Deposition of Metals in Ore-Forming Hydrothermal Systems. In *Building Exploration Capability for the 21st Century*; Society of Economic Geologists: Littleton, CO, USA, 2014; pp. 77–95.
28. Zhou, T.F.; Zhang, L.J.; Yuan, F.; Fan, Y.; Cooke, D.R. La-Icp-Ms in Situ Trace Element Analysis of Pyrite from the Xinqiao Cu-Au-S Deposit in Tongling, Anhui, and Its Constraints on the Ore Genesis. *Earth Sci. Front.* **2010**, *17*, 306–319.
29. Qiu, Z.W.; Li, Z.K.; Yuan, Z.Z. Microstructure and Trace Elements of Pyrite from Sanshandao Gold Deposit in Jiaodong District: Implications for Mechanism of Gold Enrichment. *Editor. Comm. Earth Sci. J. China Univ. Geosci.* **2022**, *47*, 290–308.
30. Feng, Y.Z.; Zhang, Y.; Xie, Y.L.; Shao, Y.J.; Lai, C. Pyrite Geochemistry and Metallogenic Implications of Gutaishan Au Deposit in Jiangnan Orogen, South China. *Ore Geol. Rev.* **2020**, *117*, 103298. [CrossRef]
31. Gao, F.; Du, Y.; Pang, Z.; Du, Y.; Xin, F.; Xie, J. La-Icp-Ms Trace-Element Analysis of Pyrite from the Huanxiangwa Gold Deposit, Xiong'ershan District, China: Implications for Ore Genesis. *Minerals* **2019**, *9*, 157. [CrossRef]
32. Luo, Z.X.; Huang, X.L.; Wang, X.; Yang, F.; Han, L. Geochronology and Geochemistry of the Ttg Gneisses from the Taihua Group in the Xiaoshan Area, North China Craton: Constraints on Petrogenesis. *Geotecton. Metallog.* **2018**, *42*, 332–347. [CrossRef]
33. Meng, J.; Li, H.M.; Li, L.X.; Li, J.R. Depositional Time of the Tieshanmiao Iron Ore Deposit in the Taihua Complex, Southern Margin of the North China Craton: Constraint from Zircon U-Pb Dating and Hf Isotope Evidence. *Acta Geol. Sin.* **2018**, *92*, 125–141.
34. Shi, M.; Yu, J.H.; Xu, X.S.; Tang, H.F.; Qiu, J.S.; Chen, L.H. U-Pb Ages and Hf Isotope Compositions of Zircons of Taihua Group in Xiaoqinling Area, Shaanxi Province. *Acta Petrol. Sin.* **2011**, *27*, 3095–3108.
35. Zhao, T.P.; Xu, Y.H.; Zhai, M.G. Petrogenesis and Tectonic Setting of the Paleoproterozoic Xiong'er Group in the Southern Part of the North China Craton:A Review. *Geol. J. China Univ.* **2007**, *13*, 191–206.
36. Jin, X.; Wang, G.; Tang, P.; Hu, C.; Liu, Y.; Zhang, S. 3D Geological Modelling and Uncertainty Analysis for 3d Targeting in Shanggong Gold Deposit (China). *J. Geochem. Explor.* **2020**, *210*, 106442. [CrossRef]
37. Li, N.; Chen, Y.J.; McNaughton, N.J.; Ling, X.X.; Deng, X.H.; Yao, J.M.; Wu, Y.S. Formation and Tectonic Evolution of the Khondalite Series at the Southern Margin of the North China Craton: Geochronological Constraints from a 1.85-Ga Mo Deposit in the Xiong'ershan Area. *Precambrian Res.* **2015**, *269*, 1–17. [CrossRef]
38. Zhang, Y.H.; Zhang, S.H.; Han, Y.G.; Zhang, H.J. Strik-Slip Features of the Machaoying Fault Zone and Its Evolution in the Huaxiong Terrane, Southern North China Craton. *J. Jilin Univ.* **2006**, *36*, 169–176+193. [CrossRef]
39. Hu, X.G. Discussion on Geological-Geochemical Characteristics and Oer-Controlling Conditions of Yanshanian Rock Mass in Xiong'ershan Ore District. Master's Thesis, China University of Geosciences, Beijing, China, 2019.
40. You, Y.Y.; Wang, X.G.; Zhao, Y.J. Geological Characteristics and Resource Potential of the Miaoling Gold Deposit, Western Henan Province. *Miner. Explor.* **2020**, *11*, 1831–1836.
41. Zhai, L.; Liu, Y.G.; Jiao, Y.H. Geological Features and Ore-Forming Age of Miaoling Gold Deposit in Henan. *Jilin Geol.* **2011**, *30*, 34–40.
42. Liu, Y.; Hu, Z.; Gao, S.; Günther, D.; Xu, J.; Gao, C.; Chen, H. In Situ Analysis of Major and Trace Elements of Anhydrous Minerals by La-Icp-Ms without Applying an Internal Standard. *Chem. Geol.* **2008**, *257*, 34–43. [CrossRef]
43. Abraitis, P.K.; Pattrick, R.A.D.; Vaughan, D.J. Variations in the Compositional, Textural and Electrical Properties of Natural Pyrite: A Review. *Int. J. Miner. Process.* **2004**, *74*, 41–59. [CrossRef]
44. Large, R.R.; Bull, S.W.; Maslennikov, V.V. A Carbonaceous Sedimentary Source-Rock Model for Carlin-Type and Orogenic Gold Deposits. *Econ. Geol.* **2011**, *106*, 331–358. [CrossRef]
45. Zhang, Y.; Shao, Y.J.; Chen, H.Y.; Liu, Z.F.; Li, D.F. A Hydrothermal Origin for the Large Xinqiao Cu-S-Fe Deposit, Eastern China: Evidence from Sulfide Geochemistry and Sulfur Isotopes. *Ore Geol. Rev.* **2017**, *88*, 534–549. [CrossRef]
46. Deditius, A.P.; Utsunomiya, S.; Reich, M.; Kesler, S.E.; Ewing, R.C.; Hough, R.; Walshe, J. Trace Metal Nanoparticles in Pyrite. *Ore Geol. Rev.* **2011**, *42*, 32–46. [CrossRef]
47. Palenik, C.S.; Utsunomiya, S.; Reich, M.; Kesler, S.E.; Wang, L.M.; Ewing, R.C. "Invisible" Gold Revealed: Direct Imaging of Gold Nanoparticles in a Carlin-Type Deposit. *Am. Mineral.* **2004**, *89*, 1359–1366. [CrossRef]
48. Sung, Y.H.; Brugger, J.; Ciobanu, C.L.; Pring, A.; Skinner, W.; Nugus, M. Invisible Gold in Arsenian Pyrite and Arsenopyrite from a Multistage Archaean Gold Deposit: Sunrise Dam, Eastern Goldfields Province, Western Australia. *Miner. Depos.* **2009**, *44*, 765–791. [CrossRef]
49. Ciobanu, C.L.; Cook, N.J.; Utsunomiya, S.; Kogagwa, M.; Green, L.; Gilbert, S.; Wade, B. Gold-Telluride Nanoparticles Revealed in Arsenic-Free Pyrite. *Am. Mineral.* **2012**, *97*, 1515–1518. [CrossRef]
50. Hou, L.; Peng, H.J.; Ding, J.; Zhang, J.R.; Zhu, S.B.; Wu, S.Y.; Wu, Y.; Ouyang, H.G. Textures and in Situ Chemical and Isotopic Analyses of Pyrite, Huijiabao Trend, Youjiang Basin, China: Implications for Paragenesis and Source of Sulfur. *Econ. Geol.* **2016**, *111*, 331–353. [CrossRef]

51. Yang, L.Q.; Deng, J.; Wang, Z.L.; Guo, L.N.; Li, R.H.; Groves, D.I.; Danyushevsky, L.V.; Zhang, C.; Zheng, X.L.; Zhao, H. Relationships between Gold and Pyrite at the Xincheng Gold Deposit, Jiaodong Peninsula, China: Implications for Gold Source and Deposition in a Brittle Epizonal Environment. *Econogeol. Mic Geol.* **2016**, *111*, 105–126. [CrossRef]
52. Li, W.; Cook, N.J.; Xie, G.Q.; Mao, J.W.; Ciobanu, C.L.; Fu, B. Complementary Textural, Trace Element, and Isotopic Analyses of Sulfides Constrain Ore-Forming Processes for the Slate-Hosted Yuhengtang Au Deposit, South China. *Econ. Geol.* **2021**, *116*, 1825–1848. [CrossRef]
53. Reich, M.; Kesler, S.E.; Utsunomiya, S.; Palenik, C.S.; Chryssoulis, S.L.; Ewing, R.C. Solubility of Gold in Arsenian Pyrite. *Geochim. Cosmochim. Acta* **2005**, *69*, 2781–2796. [CrossRef]
54. Gregory, D.D.; Large, R.R.; Halpin, J.A.; Baturina, E.L.; Lyons, T.W.; Wu, S.; Danyushevsky, L.; Sack, P.J.; Chappaz, A.; Maslennikov, V.V.; et al. Trace Element Content of Sedimentary Pyrite in Black Shales. *Econ. Geol.* **2015**, *110*, 1389–1410. [CrossRef]
55. Deditius, A.P.; Reich, M.; Kesler, S.E.; Utsunomiya, S.; Chryssoulis, S.L.; Walshe, J.; Ewing, R.C. The Coupled Geochemistry of Au and as in Pyrite from Hydrothermal Ore Deposits. *Geochim. Cosmochim. Acta* **2014**, *140*, 644–670. [CrossRef]
56. Cook, N.J.; Spry, P.G.; Vokes, F.M. Mineralogy and Textural Relationships among Sulfosalts and Related Minerals in the Bleikvassli Zn-Pb-(Cu) Deposit, Nordland, Norway. *Miner. Depos.* **1998**, *34*, 35–56. [CrossRef]
57. Bralia, A.; Sabatini, G.; Troja, F. A Revaluation of the Co/Ni Ratio in Pyrite as Geochemical Tool in Ore Genesis Problems. *Miner. Depos.* **1979**, *14*, 353–374. [CrossRef]
58. Shannon, R.D. Revised Effective Ionic Radii and Systematic Studies of Interatomic Distances in Halides and Chalcogenides. *Acta Crystallogr. Sect. A* **1976**, *32*, 751–767. [CrossRef]
59. Koglin, N.; Frimmel, H.E.; Minter, W.E.L.; Brätz, H. Trace-Element Characteristics of Different Pyrite Types in Mesoarchaean to Palaeoproterozoic Placer Deposits. *Miner. Depos.* **2010**, *45*, 259–280. [CrossRef]
60. Reich, M.; Deditius, A.; Chryssoulis, S.; Li, J.W.; Ma, C.Q.; Parada, M.A.; Barra, F.; Mittermayr, F. Pyrite as a Record of Hydrothermal Fluid Evolution in a Porphyry Copper System: A Sims/Empa Trace Element Study. *Geochim. Cosmochim. Acta* **2013**, *104*, 42–62. [CrossRef]
61. Tauson, V.L.; Kravtsova, R.G.; Smagunov, N.V.; Spiridonov, A.M.; Grebenshchikova, V.I.; Budyak, A.E. Structurally and Superficially Bound Gold in Pyrite from Deposits of Different Genetic Types. *Russ. Geol. Geophys.* **2014**, *55*, 273–289. [CrossRef]
62. Kouhestani, H.; Ghaderi, M.; Large, R.R.; Zaw, K. Texture and Chemistry of Pyrite at Chah Zard Epithermal Gold-Silver Deposit, Iran. *Ore Geol. Rev.* **2017**, *84*, 80–101. [CrossRef]
63. Shao, Y.J.; Wang, W.S.; Liu, Q.Q.; Zhang, Y. Trace Element Analysis of Pyrite from the Zhengchong Gold Deposit, Northeast Hunan Province, China: Implications for the Ore-Forming Process. *Minerals* **2018**, *8*, 262. [CrossRef]
64. Keith, M.; Smith, D.J.; Doyle, K.; Holwell, D.A.; Jenkin, G.R.T.; Barry, T.L.; Becker, J.; Rampe, J. Pyrite Chemistry: A New Window into Au-Te Ore-Forming Processes in Alkaline Epithermal Districts, Cripple Creek, Colorado. *Geochim. Cosmochim. Acta* **2020**, *274*, 172–191. [CrossRef]
65. Grundler, P.V.; Brugger, J.; Etschmann, B.E.; Helm, L.; Liu, W.; Spry, P.G.; Tian, Y.; Testemale, D.; Pring, A. Speciation of Aqueous Tellurium (IV) in Hydrothermal Solutions and Vapors, and the Role of Oxidized Tellurium Species in Te Transport and Gold Deposition. *Geochim. Cosmochim. Acta* **2013**, *120*, 298–325. [CrossRef]
66. Zhang, H.Y.; Zhao, Q.Q.; Zhao, G.; Hong, J.X.; Liu, J.J.; Zhai, D.G. In Situ La-Icp-Ms Trace Element Analysis of Pyrite and Its Application in Study of Au Deposit. *Miner. Depos.* **2022**, *41*, 1182–1199. [CrossRef]
67. Large, R.R.; Danyushevsky, L.; Hollit, C.; Maslennikov, V.; Meffre, S.; Gilbert, S.; Bull, S.; Scott, R.; Emsbo, P.; Thomas, H.; et al. Gold and Trace Element Zonation in Pyrite Using a Laser Imaging Technique: Implications for the Timing of Gold in Orogenic and Carlin-Style Sediment-Hosted Deposits. *Econ. Geol.* **2009**, *104*, 635–668. [CrossRef]
68. Maslennikov, V.V.; Maslennikova, S.P.; Large, R.R.; Danyushevsky, L.V. Study of Trace Element Zonation in Vent Chimneys from the Silurian Yaman-Kasy Volcanic-Hosted Massive Sulfide Deposit (Southern Urals, Russia) Using Laser Ablation-Inductively Coupled Plasma Mass Spectrometry (LA-ICPMS). *Econ. Geol.* **2009**, *104*, 1111–1141. [CrossRef]
69. Rottier, B.; Kouzmanov, K.; Wälle, M.; Bendezú, R.; Fontboté, L. Sulfide Replacement Processes Revealed by Textural and La-Icp-Ms Trace Element Analyses: Example from the Early Mineralization Stages at Cerro De Pasco, Peru. *Econ. Geol.* **2016**, *111*, 1347–1367. [CrossRef]
70. Tauson, V.L.; Babkin, D.N.; Akimov, V.V.; Lipko, S.V.; Smagunov, N.V.; Parkhomenko, I.Y. Trace Elements as Indicators of the Physicochemical Conditions of Mineral Formation in Hydrothermal Sulfide Systems. *Russ. Geol. Geophys.* **2013**, *54*, 526–543. [CrossRef]
71. Tauson, V.L.; Lipko, S.V.; Smagunov, N.V.; Kravtsova, R.G.; Arsent'ev, K.Y. Distribution and Segregation of Trace Elements During the Growth of Ore Mineral Crystals in Hydrothermal Systems: Geochemical and Mineralogical Implications. *Russ. Geol. Geophys.* **2018**, *59*, 1718–1732. [CrossRef]
72. Afifi, A.M.; Kelly, W.C.; Essene, E.J. Phase Relations among Tellurides, Sulfides, and Oxides; I, Thermochemical Data and Calculated Equilibria. *Econ. Geol.* **1988**, *83*, 377–394. [CrossRef]

73. Roman, N.; Reich, M.; Leisen, M.; Morata, D.; Barra, F.; Deditius, A.P. Geochemical and Micro-Textural Fingerprints of Boiling in Pyrite. *Geochim. Cosmochim. Acta* **2019**, *246*, 60–85. [CrossRef]
74. Clark, C.; Grguric, B.; Mumm, A.S. Genetic Implications of Pyrite Chemistry from the Palaeoproterozoic Olary Domain and Overlying Neoproterozoic Adelaidean Sequences, Northeastern South Australia. *Ore Geol. Rev.* **2004**, *25*, 237–257. [CrossRef]
75. Grant, H.L.J.; Hannington, M.D.; Petersen, S.; Frische, M.; Fuchs, S.H. Constraints on the Behavior of Trace Elements in the Actively-Forming Tag Deposit, Mid-Atlantic Ridge, Based on La-Icp-Ms Analyses of Pyrite. *Chem. Geol.* **2018**, *498*, 45–71. [CrossRef]
76. Migdisov, A.A.; Zezin, D.; Williams-Jones, A.E. An Experimental Study of Cobalt (Ii) Complexation in Cl^- and H_2S-Bearing Hydrothermal Solutions. *Geochim. Cosmochim. Acta* **2011**, *75*, 4065–4079. [CrossRef]
77. Skirrow, R.G.; Walshe, J.L. Reduced and Oxidized Au-Cu-Bi Iron Oxide Deposits of the Tennant Creek Inlier, Australia: An Integrated Geologic and Chemical Model. *Econ. Geol. Bull. Soc. Econ. Geol.* **2002**, *97*, 1167–1202. [CrossRef]
78. Huston, D.L.; Sie, S.H.; Suter, G.F.; Cooke, D.R.; Both, R.A. Trace-Elements in Sulfide Minerals from Eastern Australian Volcanic-Hosted Massive Sulfide Deposits 1. Proton Microprobe Analyses of Pyrite, Chalcopyrite, and Sphalerite, And 2. Selenium Levels in Pyrite—Comparison with Delta-S-34 Values and Implications for the Source of Sulfur in Volcanogenic Hydrothermal Systems. *Econ. Geol.* **1995**, *90*, 1167–1196. [CrossRef]
79. Li, X.H.; Fan, H.R.; Yang, K.F.; Hollings, P.; Liu, X.; Hu, F.F.; Cai, Y.C. Pyrite Textures and Compositions from the Zhuangzi Au Deposit, Southeastern North China Craton: Implication for Ore-Forming Processes. *Contrib. Mineral. Petrol.* **2018**, *173*, 73. [CrossRef]
80. Ulrich, T.; Long, D.G.F.; Kamber, B.S.; Whitehouse, M.J. In Situ Trace Element and Sulfur Isotope Analysis of Pyrite in a Paleoproterozoic Gold Placer Deposit, Pardo and Clement Townships, Ontario, Canada. *Econ. Geol.* **2011**, *106*, 667–686. [CrossRef]
81. Zhang, J.; Deng, J.; Chen, H.; Yang, L.; Cooke, D.; Danyushevsky, L.; Gong, Q. La-Icp-Ms Trace Element Analysis of Pyrite from the Chang'an Gold Deposit, Sanjiang Region, China: Implication for Ore-Forming Process. *Gondwana Res.* **2014**, *26*, 557–575. [CrossRef]
82. Zhai, D.; Williams-Jones, A.; Liu, J.; Tombros, S.; Cook, N. Mineralogical, Fluid Inclusion, and Multiple Isotope (H-O-S-Pb) Constraints on the Genesis of the Sandaowanzi Epithermal Au-Ag-Te Deposit, Ne China. *Econ. Geol.* **2018**, *113*, 1359–1382. [CrossRef]
83. Li, S.R.; Santosh, M.; Zhang, H.F.; Shen, J.F.; Dong, G.C.; Wang, J.Z.; Zhang, J.Q. Inhomogeneous Lithospheric Thinning in the Central North China Craton: Zircon U-Pb and S-He-Ar Isotopic Record from Magmatism and Metallogeny in the Taihang Mountains. *Gondwana Res.* **2013**, *23*, 141–160. [CrossRef]
84. LaFlamme, C.; Sugiono, D.; Thébaud, N.; Caruso, S.; Fiorentini, M.; Selvaraja, V.; Jeon, H.; Voute, F.; Martin, L. Multiple Sulfur Isotopes Monitor Fluid Evolution of an Archean Orogenic Gold Deposit. *Geochim. Cosmochim. Acta* **2018**, *222*, 436–446. [CrossRef]
85. Fan, H.R.; Xie, Y.H.; Zhao, R.; Wang, R.L. Stable Isotope Geochemistry of Rocks and Gold Deposits in the Xiongershan Area Western Henan Province. *Contrib. Geol. Miner. Resour. Res.* **1994**, *1*, 54–64.
86. Li, N.; Carranza, E.J.M.; Ni, Z.Y.; Guo, D.S. The Co_2-Rich Magmatic-Hydrothermal Fluid of the Qiyugou Breccia Pipe, Henan Province, China: Implication for Breccia Genesis and Gold Mineralization. *Geochem. Explor. Environ. Anal.* **2012**, *12*, 147–160. [CrossRef]
87. Li, N.; Chen, Y.J.; Pirajno, F.; Gong, H.J.; Mao, S.D.; Ni, Z.Y. La-Icp-Ms Zircon U-Pb Dating, Trace Element and Hf Isotope Geochemistry of the Heyu Granite Batholith, Eastern Qinling, Central China: Implications for Mesozoic Tectono-Magmatic Evolution. *Lithos* **2012**, *142*, 34–47. [CrossRef]
88. Zhao, Z.F.; Zheng, Y.F. Theoretical Calculation of Oxygen Isotope Fractionation in Magmatic Rocks. *Acta Petrol. Sin.* **1999**, *15*, 1–13.
89. Fu, Z.G.; Wong, J.C.; Lu, X.X. Sulfur Isotope Geochemical Characteristics of Gold Deposits in Xiaoqinling-Xionger Mountain Area. *Geophys. Geochem. Explor.* **2009**, *33*, 507–514+519.
90. Ohmoto, H. Stable Isotope Geochemistry of Ore Deposits. *Rev. Mineral. Geochem.* **1986**, *161*, 491–559.
91. Ohmoto, H.; Goldhaber, B. Systematics of Sulfur and Carbon Isotopes in Hydrothermal Ore Deposits. *Econ. Geol.* **1972**, *67*, 551–578. [CrossRef]
92. Wei, D.T.; Xia, Y.; Gregory, D.D.; Steadman, J.A.; Tan, Q.P.; Xie, Z.J.; Liu, X.J. Multistage Pyrites in the Nibao Disseminated Gold Deposit, Southwestern Guizhou Province, China: Insights into the Origin of Au from Textures, in Situ Trace Elements, and Sulfur Isotope Analyses. *Ore Geol. Rev.* **2020**, *122*, 103446. [CrossRef]
93. Cook, N.J. Mineralogy of the Sulphide Deposits at Sulitjelma, Northern Norway. *Ore Geol. Rev.* **1996**, *11*, 303–338. [CrossRef]

Disclaimer/Publisher's Note: The statements, opinions and data contained in all publications are solely those of the individual author(s) and contributor(s) and not of MDPI and/or the editor(s). MDPI and/or the editor(s) disclaim responsibility for any injury to people or property resulting from any ideas, methods, instructions or products referred to in the content.